UNIVERSITY OF CAMBRIDGE
DEPARTMENT OF ENGINEERING

# Pipeline-Soil Interface Testing

Author Name: Mar Giménez Fernández

Supervisor: Dr. Giovanna Biscontin

Date: 2015/2016

I hereby declare that, except where specifically indicated, the work submitted herein is my own original work.

*Signed* *Date*

# Pipeline-Soil Interface Testing

Mar Giménez Fernández
Churchill College
2015/2016

## Technical Abstract

Deepwater High Pressure High Temperature (HPHT) pipeline design for oil and gas transportation schemes relies heavily upon the axial interaction at the pipeline-soil interface. Incomplete information leads designers to implement conservative design envelopes to prevent extreme cases of uncontrolled lateral buckling and longitudinal pipeline walking during cycles of start-ups and shut-downs.

The key factors dictating pipeline-soil interface interaction are the in-situ conditions of the soil and pipeline installation, the vertical effective stress, the sliding velocity and the relative roughness between the soil and pipeline wall. Previous investigations have focused on characterising the effects of the first three of these factors. It is the aim of this study to obtain greater insight into the effects of varying the relative roughness at the interface, described by the roughness average (Ra) of the pipeline surface and the median particle size ($D_{50}$) of the soil. Recent development of the torsional shear Cam-Tor device enables replication of pipeline operational stress histories in the laboratory, mimicking cycles of shearing and consolidation occurring beneath a pipeline.

Tests have been conducted on normally consolidated soils at a constant vertical stress of 4 kPa. Five shearing cycles at a constant speed of 0.5 degrees per second with intermediate pausing stages were run for each test, alternating the direction of rotation with each cycle. Polypropylene sheet was used to model the pipeline surface, abraded with various grades of sand paper to achieve eight distinct roughness averages ranging between 0.13 μm and 21.62 μm. Two soil mixtures were sheared against the polypropylene surfaces. The first consisted of 100% kaolinite clay ($D_{50}$ = 0.7 μm). The second contained a uniform mixture of 50% kaolinite clay and 50% Hostun sand by weight ($D_{50}$ = 175 μm).

The tests carried out with 100% clay samples showed that the mechanism of failure can be detected during the first cycle of torsional resistance. Sliding failure corresponds to the lowest measured friction angle, and the highest corresponds to shear failure within the clay sample. Intermedi-

ate values show varying degrees of a combination of these two mechanisms. Increasing relative roughness generally caused an increase the frictional resistance to shearing. Discrepancies to the general trend from a small number of tests showed that for specific three-dimensional surface profiles, the rotation direction also influenced the degree of interface sliding and shear deformation occurring simultaneously.

Results show that increasing surface roughness leads to greater remoulding of the soil top layer and a larger generation of excess pore pressures. Densification and hardening of the clay occurs with pore pressure dissipation during pauses, increasing frictional resistance in successive cycles. This cyclic hardening also results in larger breakout displacements required for reaching residual frictional resistance.

The tests carried out with the mixed clay-sand samples show that the clay dominates the response. Therefore, using $D_{50}$ to calculate relative roughness and characterise the shearing behaviour fails to recognise the incompatibility of the mixture arising from the difference in grain size of three orders of magnitude.

For smooth surfaces, results show that the inclusion of sand grains in the clay matrix does not significantly increase the frictional resistance, as they are unable to maintain a gripping force at the interface. As surface roughness average increases, failure moves towards shearing within the clay, as crevices are filled. When roughness widths become compatible with sand grain sizes, a decrease in torsional resistance is observed as grains are jammed at the crevices and break up the stationary clay layer. This reinstates a degree of sliding failure.

The results obtained show that the use of relative roughness as a design parameter may not be appropriate in the context of every shearing problem. It would be of value to continue work on samples of clay-sand mixes of different proportions, and design a variety of topographies to test their compatibility with the particle sizes in the soil mixture. Targeting to specifically trigger the transitions between shearing mechanisms will reduce uncertainty in frictional resistance remnant of sliding failure and shear failure within the soil occurring simultaneously to varying degrees.

**Acknowledgements**

I would like to acknowledge the support of the Geotechnical and Environmental Research Group as a whole, as well as the help that staff and technicians at the Schofield Centre have offered me.

Dr. Matthew Kuo and Professor Malcolm Bolton provided valuable insight for the assembly of the Cam-Tor device and very kindly lent their time to instruct and advise me of the testing procedure. April Bowman provided me with continuous equipment support and excellent guidance for using GDSLAB software and for post-processing the output. Mark Smith and John Chandler supplied me with the materials requested and swiftly manufactured the disk components I required for testing. I am also very appreciative of the support provided by Alan Heaver from the Materials Research Laboratory in conducting profilometer measurements.

Lastly, I would like to thank Dr. Giovanna Biscontin for providing me with a highly enriching experience this year with invaluable supervision and direction throughout my project.

## Contents


**1 Introduction** **1**

1.1 Pipeline Operating Conditions . . . . . 1

1.2 Pipeline Buckling and Walking . . . . . 1

1.3 Pipeline Design Challenges . . . . . 3

1.4 Cam-Tor Device . . . . . 4

1.5 Motivation . . . . . 5

**2 Axial Soil Resistance** **6**

2.1 Testing Pipeline-Soil Interaction . . . . . 7

2.1.1 In-situ Considerations . . . . . 7

2.1.2 Vertical Effective Stress . . . . . 8

2.1.3 Sliding Velocity . . . . . 9

2.1.4 Relative Roughness . . . . . 10

2.2 Cam-Tor Device Past Tests . . . . . 13

**3 Apparatus and Experimental Test Procedure** **15**

3.1 Cam-Tor Device Set Up . . . . . 15

3.2 Soil Sample Selection . . . . . 16

3.3 Shearing Interface . . . . . 18

3.3.1 Material Selection . . . . . 18

3.3.2 Surface Roughening . . . . . 19

3.3.3 Profilometer Roughness Measurement . . . . . 19

3.4 Testing Schedule . . . . . 22

**4 Results and Discussion** **24**

4.1 Friction Angle versus Relative Roughness . . . . . 24

4.1.1 Soil Sample: 100% Kaolinite Clay; $D_{50}$ = 0.7 μm . . . . . 24

4.1.2 Soil Sample: 50% Kaolinite Clay, 50% Hostun Sand; $D_{50}$ = 175 μm . . . . . 25

4.2 Relative Roughness Effect . . . . . 26

4.2.1 Frictional Resistance During Shearing Cycles . . . . . 26

4.2.2 Shearing Mechanism . . . 31
4.3 Cyclic Hardening. . . . 32
4.4 Breakout Resistance . . . 34
4.4.1 Relative Roughness Effect . . . 35
4.4.2 Rotation Cycle Effect . . . 36
4.5 Shearing Direction Discrepancies . . . 36
4.6 Axial Displacement . . . 37
4.6.1 Shearing Rotations and Re-Consolidation Pauses . . . 38
4.6.2 Torque Measurement. . . . 41

**5 Conclusions 43**

**6 Recommendations for Future Work 46**

**7 References 47**

**Appendix – Risk Assessment Review 50**

# 1 Introduction

Investigation of the soil-structure interaction of subsea pipelines is a prominent research area, as advancements in the understanding of interaction parameters are swiftly incorporated into the design of deepwater High Pressure High Temperature (HPHT) pipelines to improve the safety, reliability and efficiency of oil and gas transportation schemes.

## 1.1 Pipeline Operating Conditions

HPHT pipelines are characterised by operating pressure and temperature requirements greater than 1020 atmospheres (15,000 psi) and/or 177°C (350°F). Typical operations over the design life of a HPHT pipeline require cycles of start-ups and variable duration short-term shut-ins and long-term shut-downs. The rate of fluctuation of temperature and/or internal pressure between working magnitudes and ambient conditions affects the rate of structural expansion and contraction. Consequently, the drainage condition surrounding the pipe varies, altering the axial pipe-soil frictional interaction and changing the subsequent longitudinal and lateral pipeline behaviour.

## 1.2 Pipeline Buckling and Walking

Start-up or shut-in/-down of a pipeline produces a temperature gradient along its length and leads to varying expansion or contraction respectively. The effective axial force generated is a combination between frictional forces at the soil and pipe wall interface and the pressure induced axial forces. Pipe-soil interaction causes a compressive axial force opposing the expansive or contractile axial movement, increasing cumulatively with distance from zero at the ends, which are typically free to expand.

Current design implements the use of upper and lower bound axial friction force envelopes along the pipe length to model drained and undrained axial movement responses. The upper bound is the fully constrained force, and the lower bound allows for significantly greater end expansion.

A constrained pipeline is under a greater effective force, making it more susceptible to lateral buckling. Lower friction that allows for greater expansion makes the pipeline more susceptible to walking. Design aims to control the severity of both of these phenomena. *Figure 1.1* shows the effective axial force in a short pipeline with lateral buckles (Bruton et al. 2007).

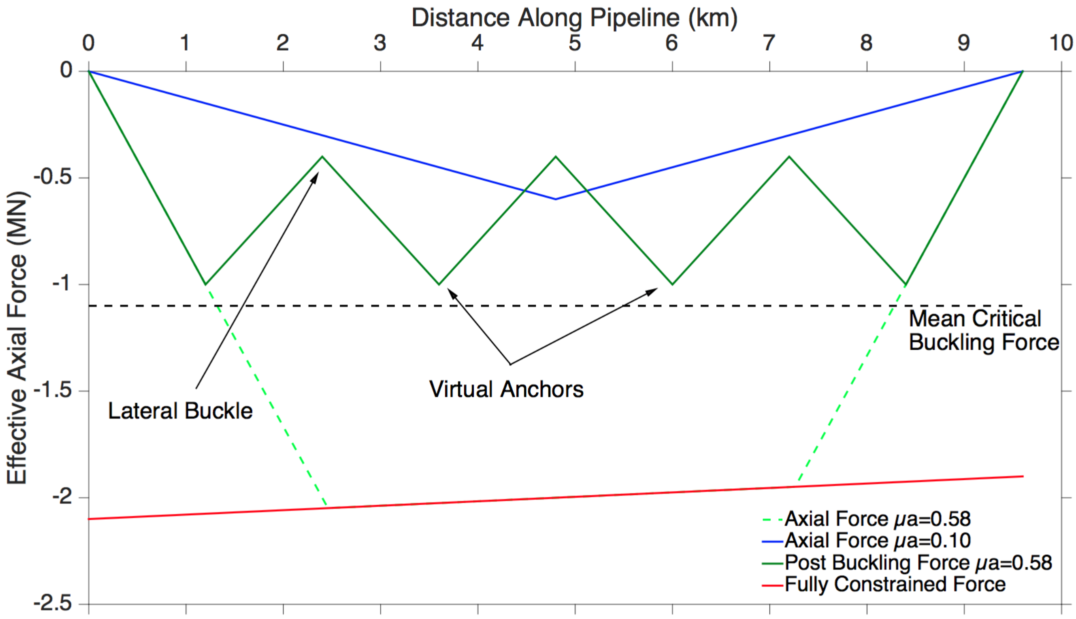


*Figure 1.1 - Effective axial force in a short pipeline with lateral buckles (Bruton et al. 2007)*

Lateral buckling instability occurs when the axial compressive force exceeds the critical buckling force, and the pipeline breaks out of its as-laid position to reduce the axial stress, as shown in *Figure 1.2*. The lateral soil resistance governs the buckled shape and therefore the bending stress of the deformed pipe. Greater resistance allows for more predictable control of buckle formation despite leading to unfavourably larger bending moments. Cyclic loading of the pipe leads to material fatigue damage from the back and forth lateral displacements over the seabed.

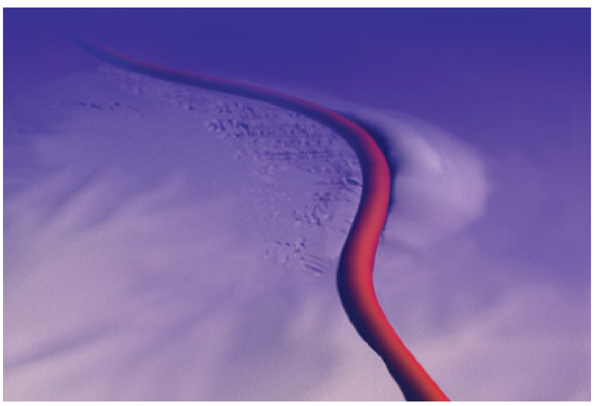

*Figure 1.2 - Lateral buckling visualization (Kaye et al. 1996)*

Pipeline walking is the global axial movement that occurs through thermal cycles when differences in axial resistance during start-up and shut-in/-down are such that the pipe does not return to its original position. This is typically associated with short pipelines, typically less than 5 km long, and occurs between lateral buckles as axial stresses are lower and unable to reach full confinement. Severe walking can lead to failure of mid-line or end connections.

## 1.3 Pipeline Design Challenges

HPHT pipeline design is very sensitive to the uncertainty in determining the axial pipe-soil resistance, as this affects the lateral buckling and axial walking behaviours and their interaction. The factors affecting the complex behaviour at the pipeline-soil interface are discussed in §2.1.

In order to overcome the inability to predict the buckled pattern that forms naturally during operation and reduce bending moments, buckle initiators are used as a means of developing controlled buckles at regular intervals, achieved by lowering lateral soil resistance. Typical techniques include incorporation of vertical upsets (rocks or pipe sleepers), local weight reductions (applied additional insulation or distributed buoyancy) or laying the pipeline in a snake-lay configuration. Pipeline anchors may be used to restrict the extent of walking. (Bruton et al. 2007, Hill and White 2015).

The design process described by Hill and White (2015), shown in *Figure 1.3*, highlights opportunities where prospective research should focus on in order to achieve improved treatment of un-

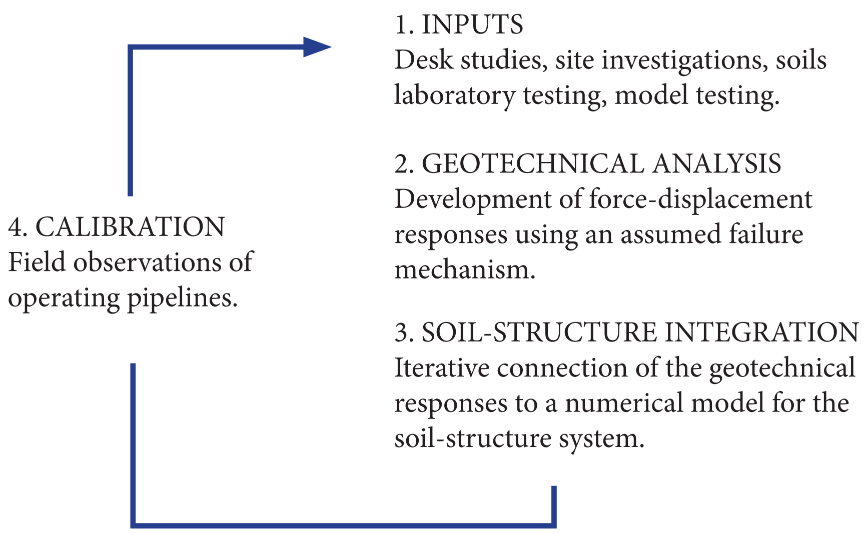


*Figure 1.3 - Pipe-soil interaction design process (Hill and White 2015)*

certainty and variability. This includes: advancement in direct in-situ measurement of pipe-soil interaction parameters, laboratory interface tests that better replicate operational stress history, improving modelling tools to understand the cyclic and large displacement effects of soil-structure interaction, and characterising differences between soil-soil and pipe-soil shearing in order to exploit beneficial mechanisms.

### 1.4 Cam-Tor Device

Kuo et al. (2015) present the Cam-Tor device, a new torsional shear instrument for interface shear testing of intact and reconstituted soil samples, developed at Cambridge University in collaboration with BP and Fugro (UK). The important results from Cam-Tor tests relevant to new experiments developed herein are discussed in §2. The mechanics and operation of this device, manufactured by GDS Instruments, are described in greater detail in §3.1.

This device is able to overcome the limitations of applying very low axial stresses and/or shearing to large strains encountered by existing shear devices including the ring shear device (Colliat et al. 2011, Lemos and Vaughan 2000), tilt tables (Pederson et al. 2003), the low stress shear box (White et al. 2012, Hill et al. 2012) and the Cam-Shear apparatus (Ganesan et al. 2014).

HTHP pipeline operational stress histories can be replicated with the Cam-Tor device by mimicking the cycles of shearing and consolidation occurring beneath the pipeline. The key features that allow for this to be achieved include:

- Ability to apply vertical stresses from 2 kPa to 50 kPa.
- Shearing at rates ranging from 0.0001 mm/s to 1 mm/s.
- Possibility of reaching any required cumulative shear displacement by running both monotonic and cyclic tests.
- Flexibility in testing a range of interface roughnesses.
- Capacity to test both natural and reconstituted soil samples.

Tests have previously been performed on two types of West African soft clay soil samples, from offshore Angola and DR Congo. These site-specific tests characterised the differences in interface friction values at different shearing rates and overconsolidation ratios (OCRs), and compared results for remoulded and intact samples.

The relationships observed were significantly influenced by the crushable pellets and marine debris found within the clay matrix (up to 42% by total dry mass), reported by Kuo and Bolton (2014b) to have unique shearing properties. Testing on natural samples is subject to variability due to heterogeneity of in-situ soil composition. Whether findings can be classed as representative when the tested specimen occupies a small volume (70 $cm^3$ in the case of the Cam-Tor device) must be carefully considered.

### 1.5 Motivation

The development of the Cam-Tor device has provided a great opportunity to obtain experimental data to develop further understanding of influencing factors on axial resistance of pipelines. It is current uncertainty and incomplete information of the soil-structure interaction taking place during HPHT pipeline operation that requires designers to implement conservative design envelopes.

Site-specific sample tests may provide key design parameters including the interface friction coefficient and the shearing mechanism taking place due to particular clay matrix characteristics. Testing on homogeneous, laboratory prepared soil samples enables reliable observations to be made of the changes in interface shearing behaviour relating to specific variation of input parameters in order to understand their dependencies.

The Cam-Tor device's testing programme capabilities and input parameters have been investigated. These include shearing soils at different rates, at a range of small magnitude vertical confining pressures, runs of monotonic shearing and cyclic tests with intermediate reconsolidation pauses. Further research may explore changes to the soil material to investigate differences between cohesive and cohesionless soils, and test them against a range of interface materials and roughnesses.

Data post-processing method improvements will aim to obtain greater time efficiency in organising the device's software output to facilitate interpretation and visualisation of the readings taken.

# 2 Axial Soil Resistance

Oliphant and Maconochie (2007) describe the peak undrained, $F_{ap}^{u}$, and peak drained, $F_{ap}^{d}$, axial resistances for soft clays with equations 1 and 2 respectively.

$$F_{ap}^{u} = A_c \cdot s_{up} \cdot \eta_p \tag{1}$$

Where $A_c$ is the contact area (depending on embedment), $s_{up}$ is the peak undrained shear strength at the pipe invert, and $\eta_p$ is the peak adhesion factor (depending on the pipeline relative roughness).

$$F_{ap}^{d} = \mu_p \cdot (W' - F_L) \tag{2}$$

Where $\mu_p = f_p\ tan\phi_p = tan\delta_p$ and $f_p$= resistance factor, $\phi_p$= peak drained angle of shearing resistance and $\delta_p$= interface friction angle. $W'$ is the operational submerged weight of the pipeline and $F_L$ is the lift force.

Data collected from a torsional shear test on the Cam-Tor device can be analysed at a characteristic radius of 0.72R, where R is the radius of the sample, to calculate the shearing friction angle. The factor 0.72 is determined by considering the average results of shear stress analysis under plastic behaviour, elastic behaviour, and by assuming an 'α' strain increase each log cycle of strain (Kuo et al. 2015).

$$\mu = \frac{\tau}{\sigma} = \frac{shear\ stress}{axial\ stress} = \frac{Torque/_{Area \times 0.72R}}{Vertical\ load/_{Area}} \tag{3}$$

The friction coefficient calculated with equation 3 will represent the soil shearing resistance or the interface friction angle depending on whether failure occurs within the soil or at the interface respectively. Possible failure mechanisms are detailed further in §2.1.4.

Peak values are required when considering breakout resistance (§2.1.1), however residual conditions may be assumed for large axial cyclic displacements (Oliphant and Maconochie 2007).

## 2.1 Testing Pipeline-Soil Interaction

Insight into the physical factors characterising the pipeline-soil interaction will serve to produce a more accurate model for the design of pipelines. The key factors dictating pipeline-soil interface interaction are the in-situ conditions of the soil and pipeline installation, the vertical effective stress, the sliding velocity and the relative roughness between the soil and pipeline wall (Kuo et al. 2015).

The subsequent descriptions of these factors outline the research observations and present conclusions made to understand their effect on axial soil resistance. Recalling the effects of each key factor will enable results affected by control variables in the tests described in §3 to be recognised.

### 2.1.1 In-situ Considerations

The top 0.5 m to 1.0 m thick layer of soil is where pipelines (carrying processed fluids) and flowlines (carrying unprocessed oil and gas mixture from well to processing facility) interact with the seabed. Accurate in-situ shear strength measurement at the soil surface is challenging to achieve with the T-bar penetrometers typically used for offshore monitoring due to initial placement penetration of the frames. The SMARTPIPE developed by Fugro in collaboration with BP and the University of Cambridge is able to directly measure pipe-soil interaction forces in three dimensions using a standardised pipe section.

An important contribution to axial resistance is the embedment of the pipeline, as a greater depth of penetration of the pipe invert relative to the undisturbed level results in a greater contact area. Greater embedment leads to a high lateral breakout restraint and thus a greater axial force required to cause buckling (Bruton et al. 2007).

A difficulty encountered with predicting as-laid embedment is that it varies spatially along the pipeline and temporally due to cycles of movement. The spatial variation occurs from a combination of slopes, irregular seabed topography, static penetration and dynamic installation effects including touchdown zone chaotic motion from vessel heave and roll or systematic stop-start movement from welding and offloading cycles. Cyclic operation described in §1.1 may also cause entrenching near the crowns of lateral buckles. Furthermore, consideration of metocean (meteorology and physical oceanography) conditions such as seabed currents or the mobility of soils combined with pipeline geometry may be required where sediment transport and scour are likely to affect embedment (Hill and White 2015, Borges Rodriguez et al. 2014).

### 2.1.2 Vertical Effective Stress

Typical normal stresses for seabed pipelines are in the range of 1 to 10 kPa. When considering this low stress range, secant strength parameters and a curved Mohr-Coulomb failure envelope are to be used, such that increasing stress levels lead to a reduction in the drained residual friction angle (Najjar et al. 2007). Normal stresses vary from a maximum at the pipeline invert to a minimum at the mudline, of which the average of the transition is used to calculate the friction ratio at the interface (Randolph et al. 2012).

The effects of vertical effective stress, including consideration of the degree of consolidation and hardening of soil, are interpreted with the Critical State Soil Mechanics Cam Clay model developed by Schofield and Wroth (1968). For normally (or lightly over-) consolidated clays, the drained shear strength is greater than the undrained shear strength. Tests show that pipeline-soil interface resistance will increase from the undrained value to the drained limit as excess pore pressures dissipate and the effective stress increases (Randolph et al. 2012).

During pipeline operation, start-ups and shut-ins/-downs cause cyclic movement of the pipeline over the seabed from a buckled to an as-laid configuration, as described in §1.1. With successive cycles, the shearing resistance of normally (or lightly over-) consolidated clays increases due to drainage. This is explained using the critical state model shown in *Figure 2.1* (Hill and White, 2015).

Undrained shearing during lateral buckling movement (§2.1.3) occurs at constant volume, as there is insufficient time for excess pore pressure dissipation (shown by the horizontal blue arrows in *Figure 2.1*). As reconsolidation occurs (red arrows), the effective stress returns to its original value at a smaller specific volume. This cyclic hardening can be thought of as an increase in apparent overconsolidation ratio (OCR) of the clay. The critical state model predicts that cyclic hardening will reach a maximum drained friction coefficient (Hill et al. 2012).

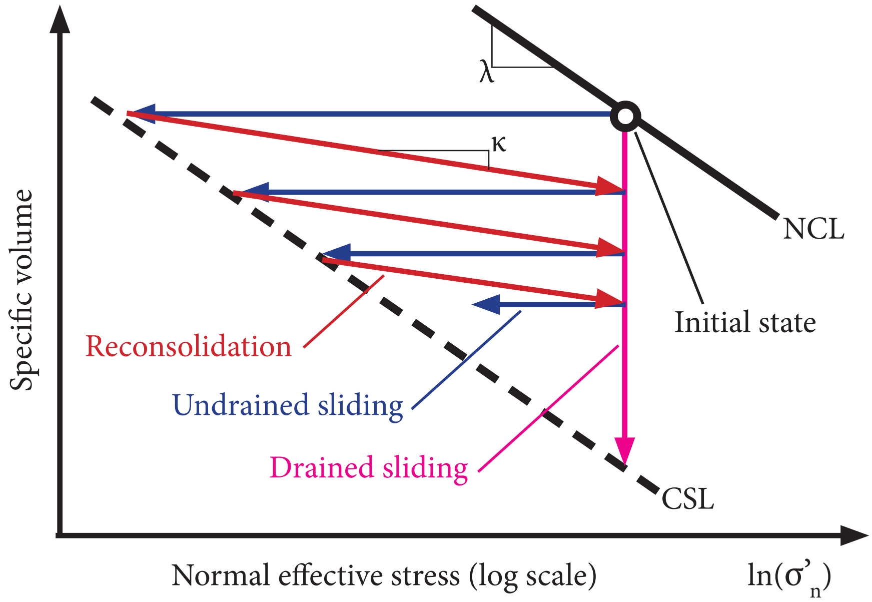


*Figure 2.1 - Cyclic hardening of axial friction: critical state model (Hill and White 2015)*

Further cycles following significant axial shearing may lead to a tendency to generate negative pore pressures due to dilation of the clay (as the apparent OCR has increased), from which a higher peak breakout frictional resistance may be observed. The global response will however be governed by residual steady state axial resistance mobilised over minute displacements (Randolph et al. 2012).

### 2.1.3 Sliding Velocity

Upper and lower bounds of interface friction will correspond to drained and undrained axial movement of the pipeline, with the rate of pore water pressure dissipation dependent on the shearing rate (Bruton et al. 2007).

Recalling from §1.2, a low axial friction allows the pipeline to be fully mobilised, leading to greater expansion and global pipeline walking. This movement therefore corresponds to undrained (or partially undrained) shearing. Axial movement may be considered as drained when the pipeline is subjected to a high axial friction but is prevented from buckling due to a high lateral resistance. Lateral breakout when buckling does occur corresponds to undrained movement.

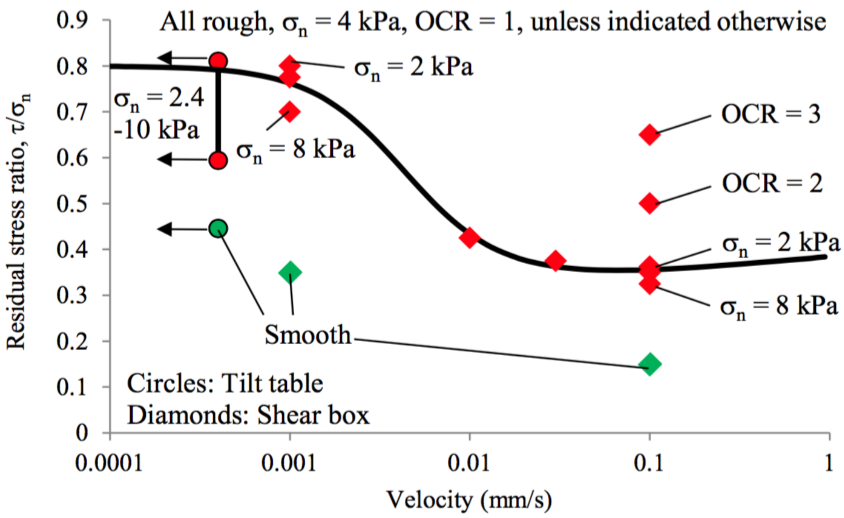


*Figure 2.2 - Element test characterisation of residual interface strength (Hill et al. 2012)*

Normally consolidated clays suffer contractive volumetric strain upon shearing, and therefore, increasing the velocity causes a reduction in frictional resistance due to the generation of positive excess pore pressure at the interface (Randolph et al. 2012).

Hill et al. 2012 produced *Figure 2.2* using interface shear box and tilt table results, showing a clear transition of interface resistance between low velocities (drained) and higher velocities (undrained) typical of pipelines during operation. The effect of cyclic hardening (§2.1.2), which can be demonstrated as an increase in OCR, can be seen to increase the friction coefficient at higher velocities (Hill et al. 2012).

### 2.1.4 Relative Roughness

The relative roughness (R) is a parameter that compares the roughness average (Ra) of the surface and the median grain size of the soil sample ($D_{50}$), as shown in equation 4 (Oliphant and Maconochie, 2007).

$$R = \frac{R_a}{D_{50}} \tag{4}$$

Roughness average is a measure of the arithmetic mean of the absolute departures of the roughness profile from the mean line. This 2D parameter is calculated by integrating the absolute value of the roughness profile over the length evaluated, given by equation 5 and shown in *Figure 2.3.*

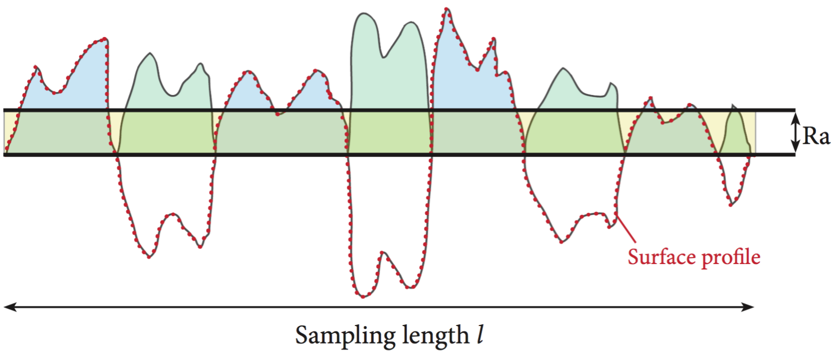


*Figure 2.3 - Surface profile roughness average depiction*

*(Image adapted from http://www.olympus-ims.com/en/knowledge/metrology/roughness/2d_parameter/ )*

$$R_a = \frac{1}{l}\int_0^l |Z(x)|\ dx \tag{5}$$

It is important to note that surfaces may have the same value of Ra but have significantly different profiles due to relative magnitudes of peaks and valleys and the differences in spacing in between. In addition, the roughness lay direction and waviness profile will influence the shearing mechanism.

Meyer et al. (2015) describe a series of direct shear interface tests using propylene interface blocks of three different roughnesses; the first without surface treatment, the second sand blasted and the third machined. Results show a trend of increasing friction angle and scatter with increasing surface roughness.

Randolph et al. (2012) and Meyer et al. (2015) use the power law relationship presented in equation 6 to relate the friction factor and the normal stress level, scaled with factors to account for the interface roughness, shown in equation 7, and the shearing rate, which represents the transition from drained to undrained conditions.

$$\frac{H}{V} = \mu = f_{rate} \cdot f_{roughness} \cdot a \cdot \sigma_n^{b-1} \tag{6}$$

$$f_{roughness} = 0.6 + \frac{0.4}{1+2.2 \cdot R_a{}^{-1.2}} \tag{7}$$

Equations 6 and 7 predict that increasing the surface roughness will cause the roughness factor to converge to a value equal to one, diminishing its effect on the friction factor. *Figure 2.4* shows a plot of the relationship expressed in equation 7 and the location of the three surfaces tested by Meyer et al. (2015) mentioned above. Constants 'a' and 'b' are taken as 0.82 and 0.86 respectively.

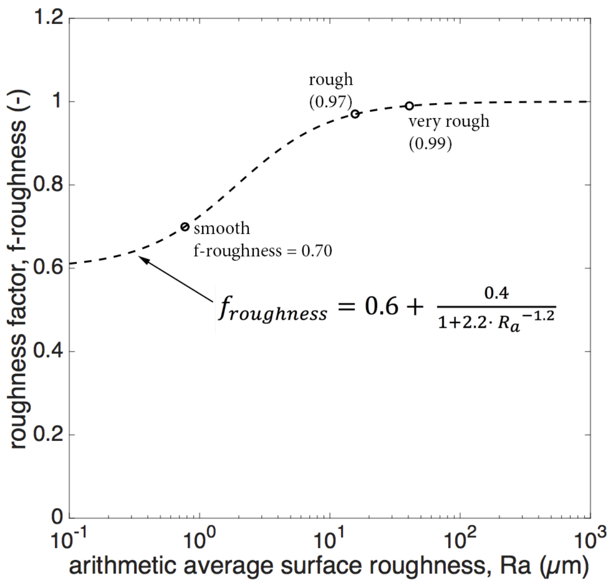


*Figure 2.4 - Roughness factor vs. average surface roughness Ra (Meyer et al. 2015)*

Oliphant and Maconochie (2007), describe the relationship between the particle size of the soil sample and the relative roughness of the interface with the predicted idealised mode of shearing failure, shown in *Figure 2.5*. The three modes of failure described are:

- Mode I: Shear failure within the soil
- Mode II: Full sliding at the interface
- Mode III: Simultaneous shear deformation and interface sliding

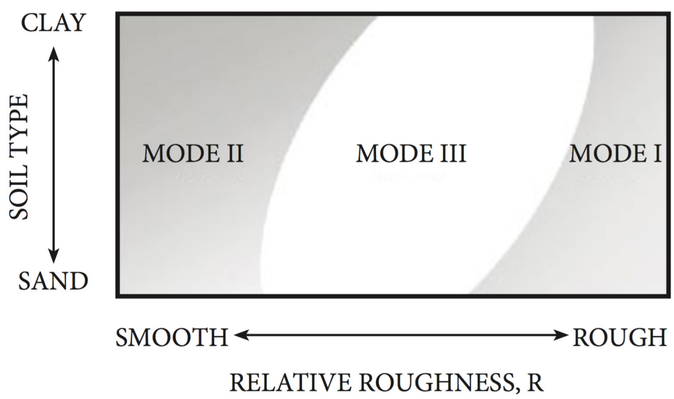


*Figure 2.5 - Idealised failure modes (Oliphant and Maconochie, 2007)*

Kuo et al. (2015), conducted tests on West African soft clay soil samples, as mentioned in §1.4, which contained crushable pellets. With consecutive shearing stages using the Cam-Tor device, Particle Image Velocimetry (PIV) analysis showed a reduction in grain size in the shear zone by an order of magnitude as the foraminifera crushed. The mechanism transitioned from interlocking of grains dominating to a greater tendency for sliding, reducing the thickness of the shear band from 2 mm to 1 mm as fewer grains become involved.

## 2.2 Cam-Tor Device Past Tests

The greatest limitation encountered with the experimental procedure involving the Cam-Tor device (as well as past direct shear tests) is the difficulty in measuring changes in pore pressures at the shearing interface. There is therefore a lack of reliable knowledge of the drainage condition during tests performed at different shearing rates.

An attempt to incorporate a pore water pressure transducer (PPT) has been made for the Cam-Tor device, by embedding the PPT into the interface material behind a porous plastic at the characteristic radius. The results were found to be unrepresentative of the pore pressures expected, owing to dampening occurring in the transmission of pore water pressures through the porous stone surrounding the PPT.

Field problems are multidirectional, with drainage and consolidation occurring in three-dimensional space. The boundary conditions are difficult to establish due to the unpredictable in-situ conditions, and therefore one-dimensional approximations are typically used in laboratory testing. Oliphant and Maconochie (2007), describe that the error in this simplification is not as significant as assumptions made about drainage path lengths and soil parameters, and is therefore appropriate.

One-dimensional consolidation using the Cam-Tor device is achieved by applying a uniform vertical pressure (§3.1). Past tests verify that sample consolidation occurs via one-way drainage through the bottom of the sample (opposite side of the sample to the shearing interface), despite the presence of a 1 mm gap around the circumference of the interface allowing for a small amount of soil extrusion (preventing excessive confining pressures from skewing compressive stress measurements). Oedometer tests carried out to derive a primary consolidation curve and determine soil compression properties therefore assume a drainage path equal to the sample height.

The effect of OCR has also been tested, to compare the results of samples with tendencies to either contract or dilate as predicted by the Critical State Soil Mechanics Cam Clay model developed by Schofield and Wroth (1968). The three OCRs testes were 1, 3 and 6. The observations were influenced by the crushable particle structures of the faecal pellets present in the sample. The increase in OCR from 1 to 3 did not show an increase in the interface friction factor consistent with a greater soil density, due to what was assumed to be the result of the change in mechanism to particle sliding explained in §2.1.4.

The Cam-Tor device also tested the effect of shearing rate on the West African soft clay soil samples, showing that residual resistances were greater during drained shearing compared to undrained. Velocities of 0.001 mm/s were assumed to produce drained results, though this could not be verified as pore pressure measurement was unobtainable. Fast shearing of 0.1 to 0.5 mm/s showed three distinct features during torsional shearing; an initial peak demonstrating the breakout resistance, a fall in strength to undrained residual shearing, and a gradual gain in resistance as pore pressures dissipate.

The phenomenon of cyclic consolidation hardening is also captured with the Cam-Tor device through tests comparing residual frictional resistance when shearing directions are reversed with and without intermediate pauses for consolidation.

Finally, there has been an interest to identify the role of relative roughness on interface friction, and a testing sequence on the Cam-Tor device with a range of three surface roughnesses gave relative interface frictional resistances of $\mu_{smoothest} < \mu_{roughest} < \mu_{intermediate}$ (Min, 2015). These results are inconsistent with the theory presented in §2.1.4. This may be demonstrating changes in the shearing mechanism or transitions in frictional behaviour different to the idealised modes described by Oliphant and Maconochie (2007), due to the crushable nature of the samples tested. A limited roughness range was examined for the tests to be conclusive, making this an appealing area for further detailed study.

# 3 Apparatus and Experimental Test Procedure

## 3.1 Cam-Tor Device Set Up

The Cam-Tor device is an interface shear tester, shown in *Figure 3.1*. The components include a constant rate of strain (CRS) consolidation cell with a base pedestal of infinite rotation capacity, and an internal load cell capable of measuring the axial force applied to the soil specimen and the torque generated from the sample rotating against the interface.

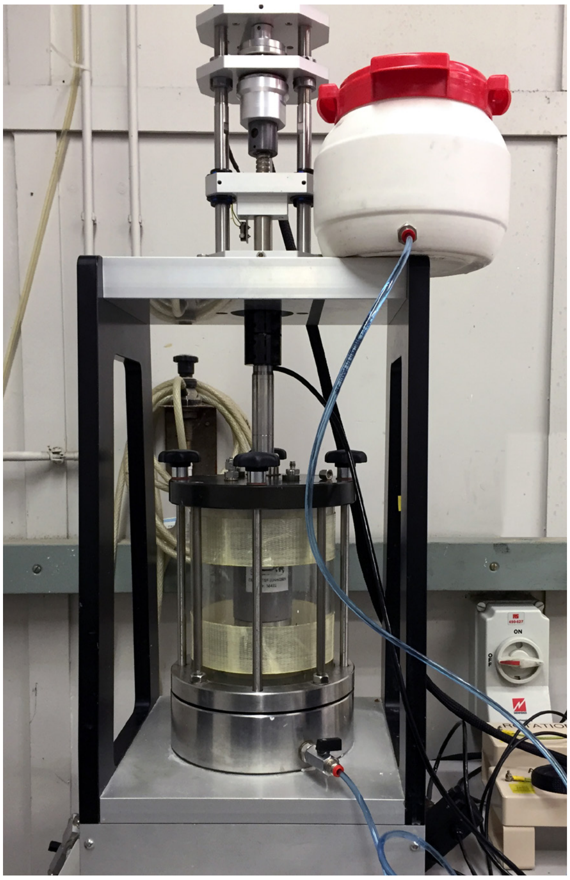

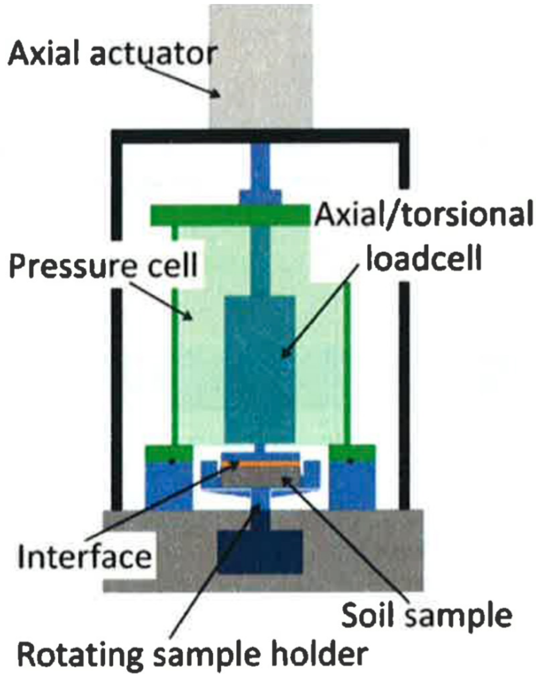


*Figure 3.1 - Cam-Tor device*

*(left) - Photograph of the laboratory set-up*
*(right) - Schematic diagram (Kuo et al. 2015)*

The device uses electro-mechanical control of the force actuator to apply the axial stress. The maximum force and torque ratings for the load cell are 200 N and 20 Nm respectively. The load cell has an accuracy of 0.1% of the full range output, and therefore the accuracy of the load applied is ±0.2 N. Tests carried out at 4 kPa (§3.4) have an axial applied load error of 1.3%.

The soil sample within the rotating holder has a 70 mm diameter, and the interface diameter is 68.5 mm. The small gap allowing for soil extrusion is essential to prevent apparatus jamming or contact between the sample holder and the interface (due to the slight vertical misalignment of the actuator), which would interfere with results. The soil sample has an 18 mm height.

The internal submersible load cell allows interface friction measurements to be made without introducing errors by the seal friction on the ram. *Figure 3.2* shows a close-up of how the top cap, onto which the interface will be bonded, fits within the sample holder.

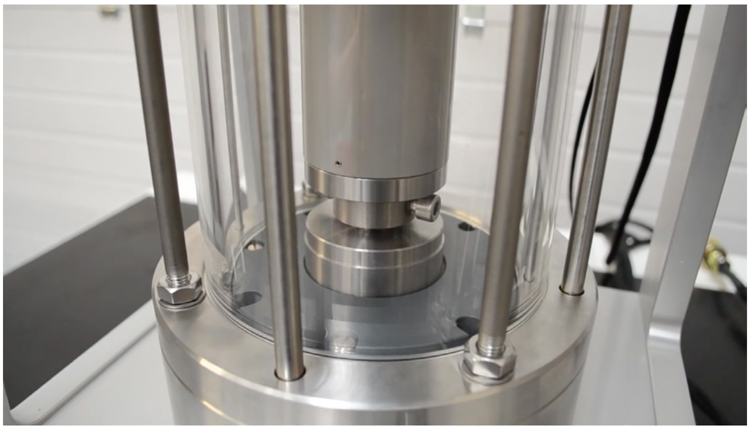

*Figure 3.2 - Close-up photograph of Cam-Tor device (http://www.gdsinstruments.com/gds-products/interface-shear-tester )*

The Cam-Tor device is controlled via the GDSLAB control and data acquisition software. Inputs to the program control the axial force applied to the soil sample with the axial actuator movement and the rotation of the base pedestal as required on a specific test. Relevant to this experiment are tests of consolidation and multi-stage constant rate rotation at constant vertical stress with intermediate pauses for reconsolidation (details are provided in §3.4).

### 3.2 Soil Sample Selection

The constituents used to make up the soil samples used in the tests described herein include kaolinite clay and Hostun sand. These materials have been selected due to the abundant literature available describing their physical properties and shearing characteristics. This allows for easier interpretation of the shearing mechanisms mobilised during testing on the Cam-Tor device for a more robust characterisation of the influence of varying relative roughness. The samples are prepared in the laboratory and should therefore not be used for site-specific design purposes.

Imerys Speswhite™ consists of highly refined kaolin of ultrafine particle size, characterised by its lamellar particle structure and chemical inertness. The median grain size of the hydrous kaolin used is $D_{50}$ = 0.7 μm, with a liquid limit of LL = 51.4%. Tsuchida and Gomyo (1995) conducted a survey of sea floor clay samples at numerous seaports to determine that typical surface marine clays have water contents of 1.5 to 2.0 times the liquid limits. The average water content of the samples tested containing only kaolinite is 103.5% (with a variance of 0.1%).

Fugro Geoconsulting UK, who have collaborated in the development of the Cam-Tor device and the testing programmes previously completed, continue to show interest in obtaining more experimental results. Liaison has highlighted their interest in shearing sandy soils against the solid interface, and hence the Hostun sand has been incorporated into the test plan. Particle size distribution of the hostun sand used in this study, analysed by the conventional sieve method established in ASTM D6913, reveals a median grain size of $D_{50}$ = 350 μm. The sand is air-dried, poorly graded, and with grains of sub-angular shape.

Two soil mixtures are sheared against the solid interface. The first consists of 100% kaolinite clay ($D_{50}$ = 0.7 μm). The second contains a uniform mixture of 50% kaolinite clay and 50% Hostun sand by weight ($D_{50}$ = 175 μm), with average water content of 57% (variance 0.01%) achieving the same consistence as the first soil mixture. Photographs of a prepared testing specimen of each mixture are shown in *Figure 3.3*.

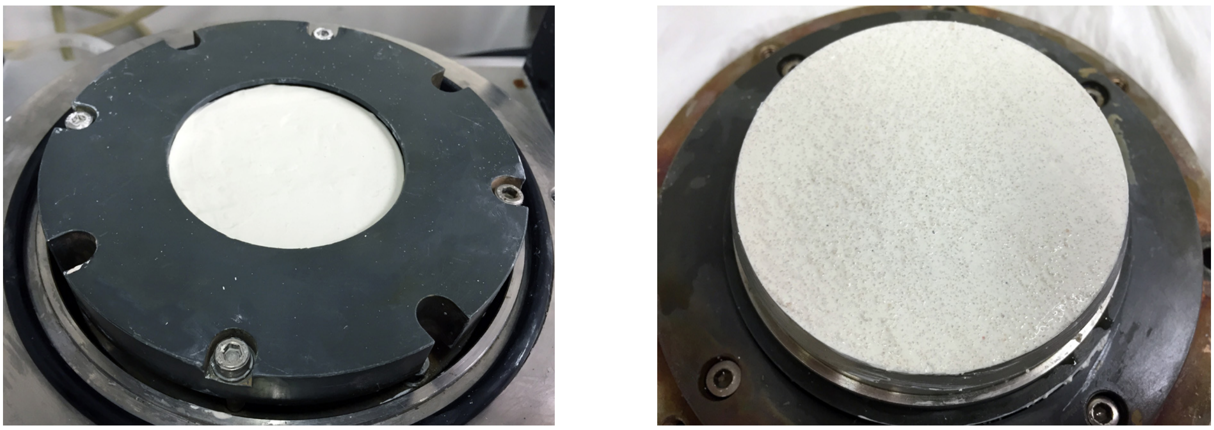

*Figure 3.3 - Photographs of soil samples prepared for testing*
*(left) - 100% kaolinite clay*
*(right) - 50% kaolinite clay, 50% Hostun sand by weight*

## 3.3 Shearing Interface

The median grain size of each mixture is used to calculate the surface roughness average that will provide the required range of relative roughnesses for testing. For these values, sandpapers with appropriate grit ratings are selected and passed over the interface material to etch and texturize the surfaces for each of the scheduled tests. A profilometer is used to verify the interface roughnesses.

### 3.3.1 Material Selection

High temperature oil and gas offshore pipelines have polypropylene (PP) three-layer external corrosion coating systems. A number of important material advantages provided by PP include:

- High impermeability; providing superior isolation from sea water.
- Excellent corrosion resistance; extending the lifetime in corrosive soils.
- Flexibility; for bending capacity during laying operations.
- Strong adhesion to steel.
- Quality assurance during manufacture method by hot extrusion providing a continuous and uniform thickness profile.

Axial pipe-soil interaction friction parameters tested by Meyer et al. (2015) were conducted using PP interface blocks with three distinct roughnesses (§2.1.4). This investigation is developed further with the experiments described herein by similarly shearing soils against PP surfaces.

The Cam-Tor device load actuator applies a uniform stress on the sample via a metal top cap, onto which discs of the desired interface material are screwed. Disks have been manufactured within the laboratory from spare aluminium parts for each of the tests outlined in §3.4. PP sheet was bonded on the surface in contact with the soil sample.

The 3 mm thick PP sheet material procured for this investigation has a Rockwell hardness of R79, a tensile strength of 27 MPa and is able to withstand a maximum long-term service temperature of 110 °C.

### 3.3.2 Surface Roughening

Uniform surface average roughnesses in two orthogonal directions are achieved by scratching the PP surfaces in a straight cross hatch pattern. As shearing occurs by circular rotation of the sample in the base pedestal against the surface, this pattern achieves the smallest variation in the shearing condition from the centre to the outer circumference.

The roughnesses attained with the different abrasive tools used are summarised in *Table 3.1*. The 'No scratch' listed tool corresponds to the smooth PP surface as received from the supplier. The 'P' grades correspond to sandpapers of different grit sizes following the Federation of European Producers of Abrasives (FEPA) classifications, with decreasing values indicating coarser finishes. The last tool listed is a bi-metal hacksaw blade with 24 teeth per inch.

| Abrasive Tool | Surface Roughness, Ra (μm) |
|---|---|
| No scratch | 0.092 |
| P1600 | 0.192 |
| P1200 | 0.514 |
| P800 | 0.660 |
| P600 | 1.104 |
| P100 | 4.557 |
| P60 | 7.686 |
| Hack saw blade 24 TPI | 15.136 |

*Table 3.1 - Roughnesses achieved with range of abrasive tools*

### 3.3.3 Profilometer Roughness Measurement

A Taylor Hobson Precision Form Talysurf profilometer was used to determine the interface roughnesses of the interfaces listed in *Table 3.1*. This equipment is a stylus profilometer, and works by physically moving a probe across the surface and measuring the force feedback from the surface pushing up in order to acquire the height profile. This is shown in *Figure 3.4*. The stylus tip size influences the measurements by limiting the resolution. The noise in roughness measurement Rq (root-mean-squared roughness) is less than 2 nm and for Rz (average peak to valley height) the measurement noise is less than 10 nm. Ra is a parameter obtained by filtering.

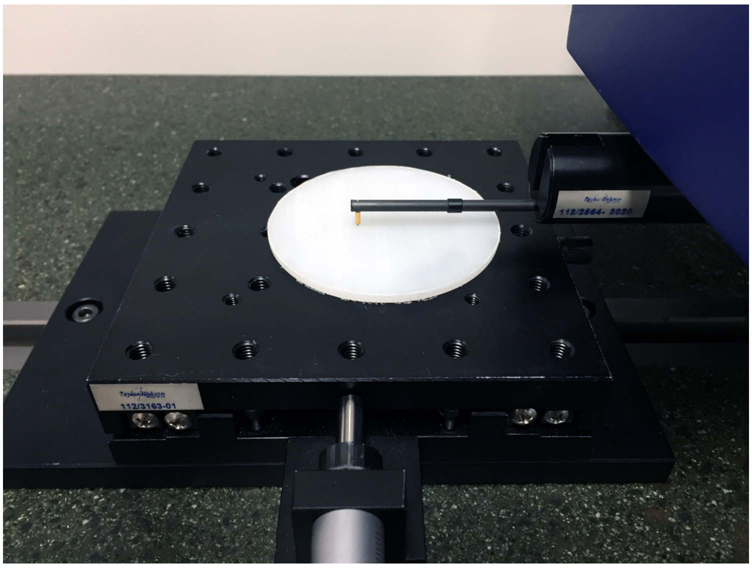


*Figure 3.4 - Photograph of profilometer probe moving across PP interface*

*Figures 3.5, 3.6, 3.7* and *3.8* show the measured surface profiles for the smooth no scratch surface, the surfaces abraded with P1200 and P100 sandpaper, and the surface etched by the hack saw blade. It is important to note the differences in scale of the vertical axes when comparing the surfaces. In these instances, the surfaces with smaller values of Ra have smaller relative roughness widths and larger relative roughness heights (conceptually sketched in *Figure 3.9*). This can be appreciated by comparing Rz and Ra values, which give ratios of 10.2, 8.2, 8.0 and 5.5 in these four cases.

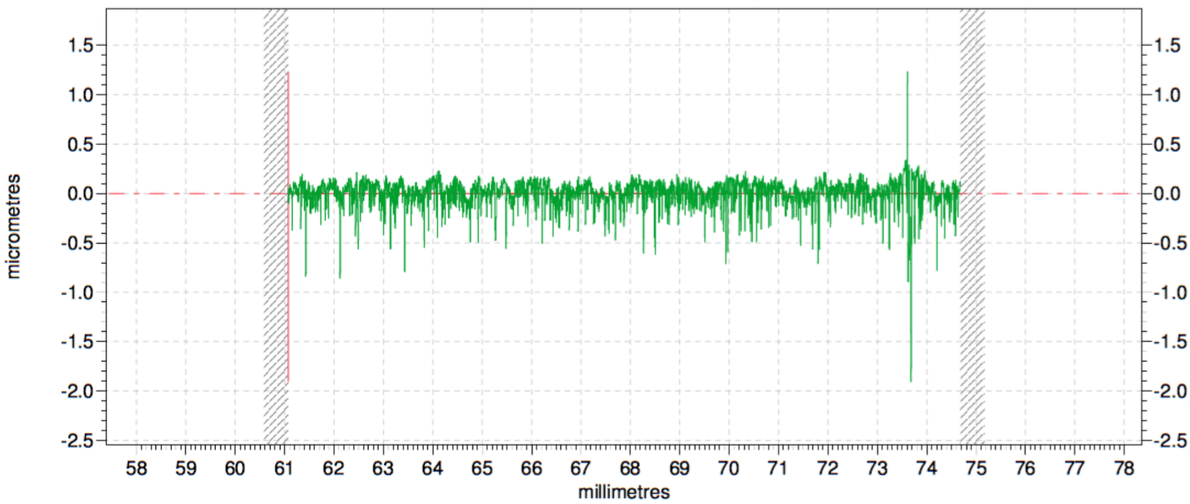


*Figure 3.5 - PP surface profile, case: No scratch, Ra=0.092μm, Rq=0.139μm, Rz=0.935μm*

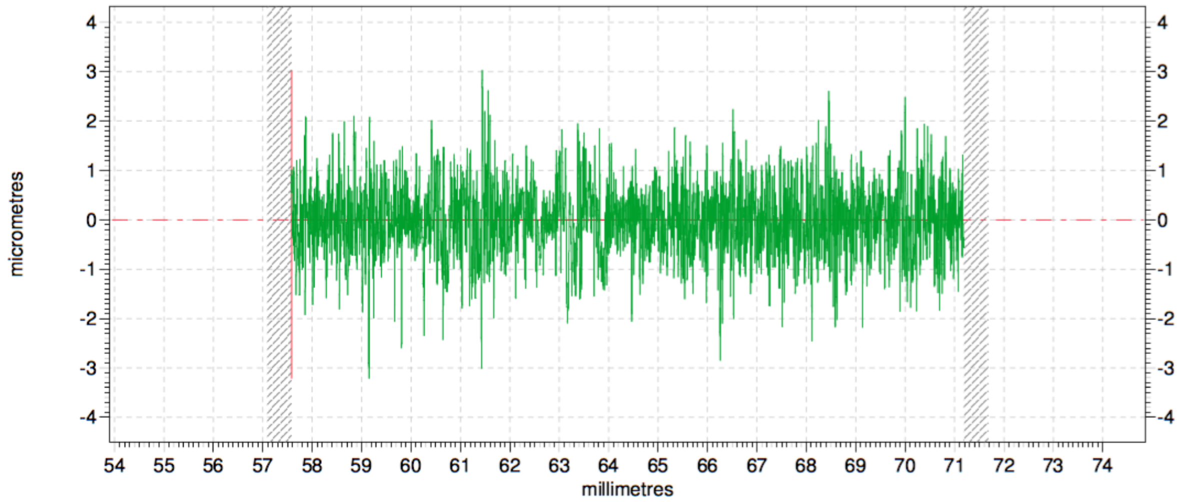

*Figure 3.6 - PP surface profile, case: P1200, Ra=0.514µm, Rq=0.674µm, Rz=4.223µm*

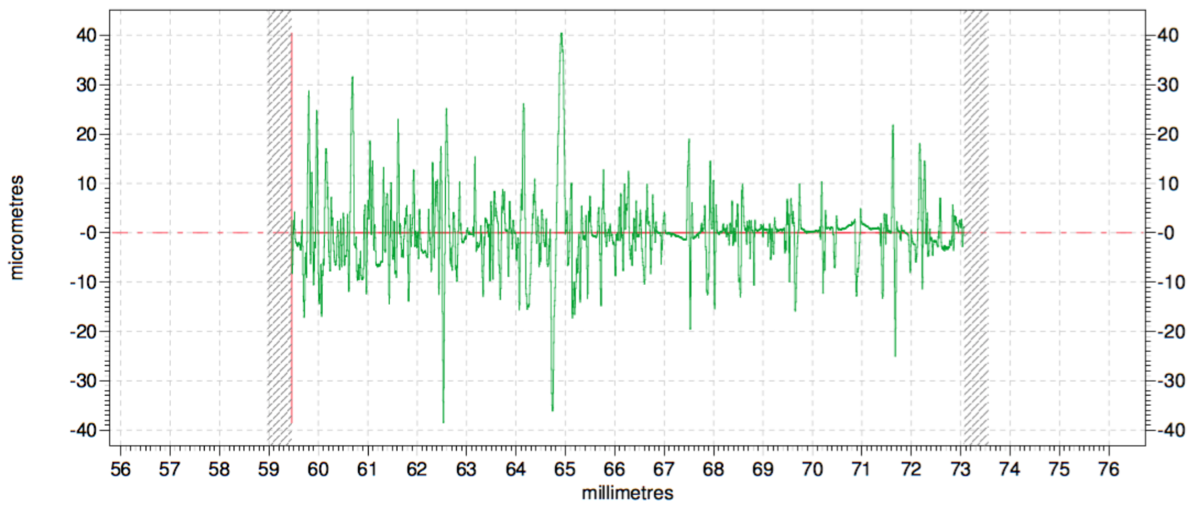

*Figure 3.7- PP surface profile, case: P100, Ra=4.557µm, Rq=7.444µm, Rz=35.296µm*

*Figure 3.8 - PP surface profile, case: Hack saw blade 24 TPI, Ra=15.137µm, Rq=21.598µm, Rz=84.026µm*

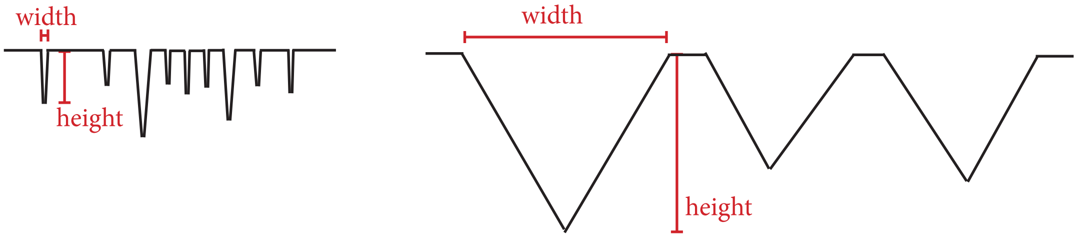


*Figure 3.9 - Schematic interpretation of surface profiles of smaller Ra (left) and larger Ra (right)*

## 3.4 Testing Schedule

*Table 3.2* shows the relative roughnesses tested with the Cam-Tor device. The same testing sequence is applied to all of the soil-PP combinations listed, in order to yield comparative results and observe the influence of varying the interface relative roughness.

| Surface Ra (μm) | Relative Roughness R | |
|---|---|---|
| | $D_{50}$ = 0.7 μm | $D_{50}$ = 175 μm |
| 0.092 | 0.13 | 0.0005 |
| 0.192 | 0.27 | - |
| 0.514 | 0.73 | - |
| 0.660 | 0.94 | - |
| 1.104 | 1.58 | 0.0063 |
| 4.557 | 6.51 | 0.0260 |
| 7.686 | 10.98 | 0.0439 |
| 15.136 | 21.62 | 0.0865 |

*Table 3.2 - Relative roughnesses (soil-PP combinations) tested*

The testing sequence goes through the following stages, all carried out at a constant compressive axial stress of 4 kPa:

1. First one-dimensional consolidation for 1830 minutes.
2. Clockwise rotation at 0.5 degrees/second for 60 minutes (1800 degrees total).
3. Reconsolidation pause between shearing stages for 30 minutes.
4. Anti-clockwise rotation at the same rate and for the same duration followed by a reconsolidation pause as before.
5. Repeated cycles of shearing and intermediate pauses for a total of 5 shearing stages.

Sample dimensions, running times, rotational control, desired speed, input stress levels and the option for pausing between shearing stages are programmed into the GDSLAB software before testing for the entire sequence to run automatically between stages, and identically for different test samples.

The software offers two options for the reconsolidation pauses:

- To target zero torque, relieving the strain in the shear zone by a slight backwards rotation; or
- To target zero rotation, stopping the sample and allowing stains to decrease over time with the dissipation of excess pore pressures generated during shearing.

In-situ site condition uncertainty makes prediction of the most representative option difficult to recognise. The second option is selected in this testing schedule to compare differences in the pore pressure generated during each consecutive shearing cycle.

# 4 Results and Discussion

## 4.1 Friction Angle versus Relative Roughness

*Figures 4.1 and 4.2* show a summary of the torsional resistance results obtained in all of the shearing tests performed, separately for the two types of soil samples tested. The plotted friction angles are obtained by calculating the mean of the values measured over rotational displacements from 360 to 1800 degrees during each cycle, thereby representing residual values. A detailed analysis of frictional changes occurring during shearing cycles, observed in *Figures 4.1 and 4.2*, is provided in the sections that follow.

### 4.1.1 Soil Sample: 100% Kaolinite Clay; $D_{50}$ = 0.7 μm

*Figure 4.1* shows the key features that result from varying the relative roughness between the PP surface and soil materials. The lines joining the plotted points are logarithmic interpolations drawn for ease of visualisation. Increasing the relative roughness leads to a greater increase in frictional resistance with each shearing rotation cycle, seen by the increasing spread of friction angles caused by cyclic hardening.

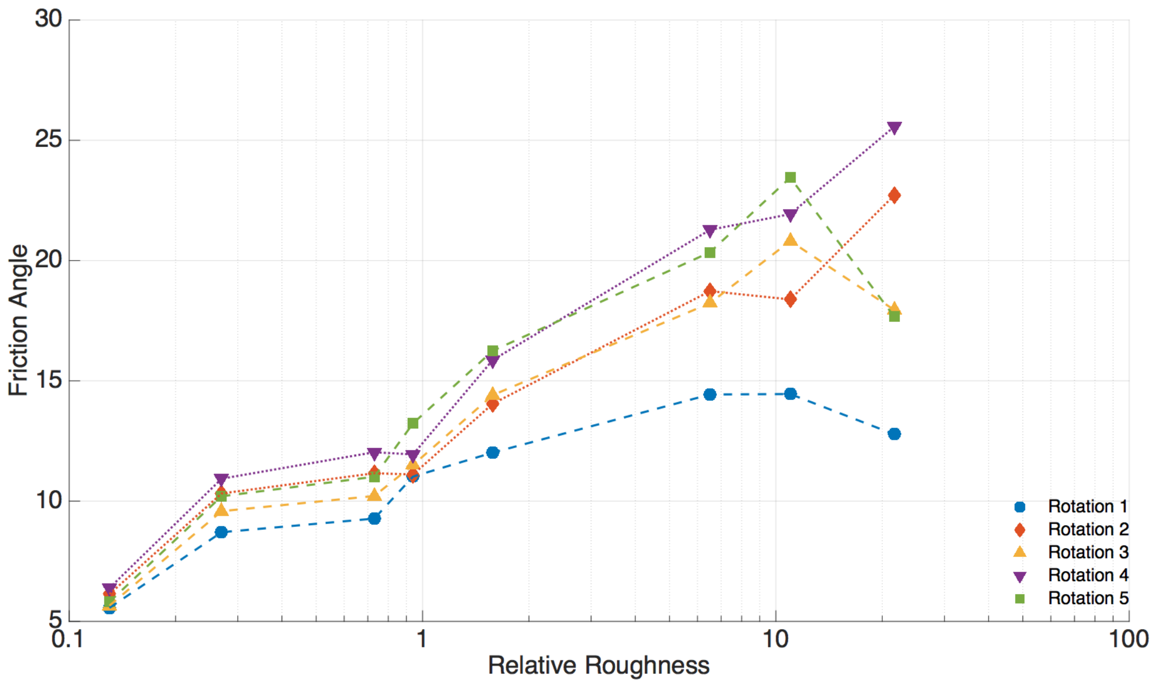


*Figure 4.1 - Friction angle versus relative roughness for each rotational shearing cycle of 100% kaolinite clay soil samples ($D_{50}$ = 0.7 μm)*

Rotations 1, 3 and 5 are all in the same direction, whereas rotations 2 and 4 cause shearing in the reverse sense. Dissimilarities can be observed between the frictional responses when the shearing direction reverses, as in five of the eight tests, rotations 2 and 4 exhibit greater resistances than successive cycles that have undergone a greater degree of cyclic hardening.

Excluding the relative roughnesses at either extreme of the tests, the trend follows the relationship predicted in *Figure 2.4*. Although *Figure 2.4* shows the influence of R on a friction factor, the only parameter varied (in equation 6) during the tests run with the Cam-Tor device shown in *Figure 4.1* is R, and therefore the relationship is expected to resemble the trend described by Meyer et al. (2015). Cyclic hardening maintains the form of the predicted behaviour, with an increase in the vertical spread.

### 4.1.2 Soil Sample: 50% Kaolinite Clay, 50% Hostun Sand; $D_{50}$ = 175 μm

The range of relative roughnesses shown in *Figure 4.2* is up to three orders of magnitude smaller than in *Figure 4.1*, for which Meyer et al. (2015) predict that there will be no discernable effect caused to the frictional resistance. This is not what the experimental data suggests, because using a median grain size in this case, where the difference in particle size is of approximately three orders of magnitude, fails to recognise incompatibility between sand grains and the clay matrix.

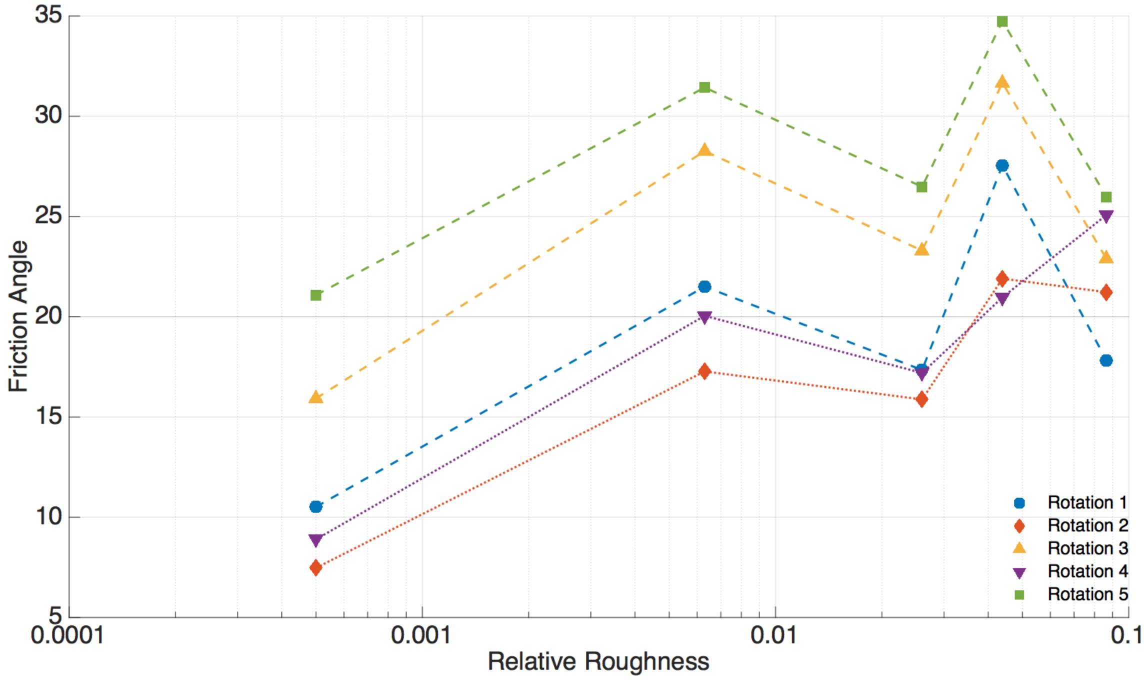


*Figure 4.2 - Friction angle versus relative roughness for each rotational shearing cycle of 50% kaolinite clay, 50% Hostun sand soil samples ($D_{50}$ = 175 μm)*

Contrary to *Figure 4.1, Figure 4.2* shows a reducing spread of friction angle with cyclic hardening for increasing values of R. Larger values of R for the soil samples with $D_{50}$ = 175 μm could not be achieved with the abrasive methods described in §3.3.2, and therefore the evolution of this trend cannot be verified.

Clay particles appear to be dominating the response, as friction values are comparable with those obtained for tests on 100% kaolinite clay soils, despite the $D_{50}$ value suggesting relative roughnesses of up to three orders of magnitudes smaller. Due to the presence of the Hostun sand in the soil mixture, there is nevertheless a general increase in friction angle measurements. The gap allowing for soil extrusion, described in §3.1, is relatively tighter for sand grains than for clay particles. There will therefore also be additional torsional restraint around the circumference of the interface disk heightened by contact with the sand particles being expelled outwards.

The change in frictional resistance with R for this soil mixture is less clear than for the 100% kaolinite clay sample, owing to the fluctuations caused by strength reductions observed in tests with R = 0.0260 and R = 0.0865.

Interestingly, the opposite behaviour with shear direction reversal occurs compared to observations from *Figure 4.1*, as torsional resistance during cycle rotations 2 and 4 are smaller than rotations 1, 3 and 5. This may be a result of full sliding at the interface, as described by Oliphant and Maconochie (2007) failure Mode II, during reversal.

## 4.2 Relative Roughness Effect

### 4.2.1 Frictional Resistance During Shearing Cycles

*Figures 4.3 and 4.5* show the results obtained for the first and fifth cycles of $D_{50}$ = 0.7 μm shearing. There appear to be distinct bands of friction angle groupings measured, highlighting changes in shearing mechanisms. Successive cycles increase the friction angle and spread between different relative roughnesses. With increasing R, the measurement of friction angle also becomes noisier.

Considering the test for full sliding at the interface corresponding to R = 0.13, *Figure 4.3* shows a gradual decay in frictional resistance from the onset, over the first 250 degrees of rotational displacement (equivalent to 108 mm at the characteristic radius), indicative of yielding behaviour up to the residual state. Comparison with the other tests shown in *Figure 4.3* shows that shearing with greater interface roughnesses requires a much smaller mobilisation distance for failure.

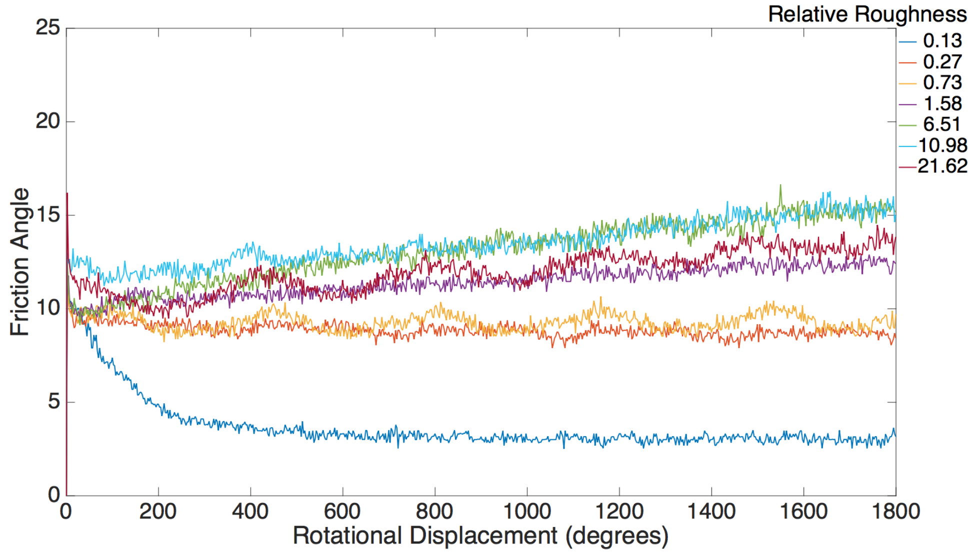


*Figure 4.3 - Plot showing change in shearing friction angle during 1st rotation cycle for the variety of relative roughnesses tested ($D_{50}$ = 0.7 μm)*

The top layer of soil, remoulded by shearing to a lower residual strength, is extruded at the outer perimeter during each shearing cycle, as depicted in *Figure 4.4*. This consequently causes an increase in torsional resistance as the stronger normally consolidated soil below is introduced into the shearing zone. This can be observed in *Figure 4.3* by the gradual increase in friction angle with increasing rotational displacement. The slope of this increase can be seen to be more significant with greater relative roughness.

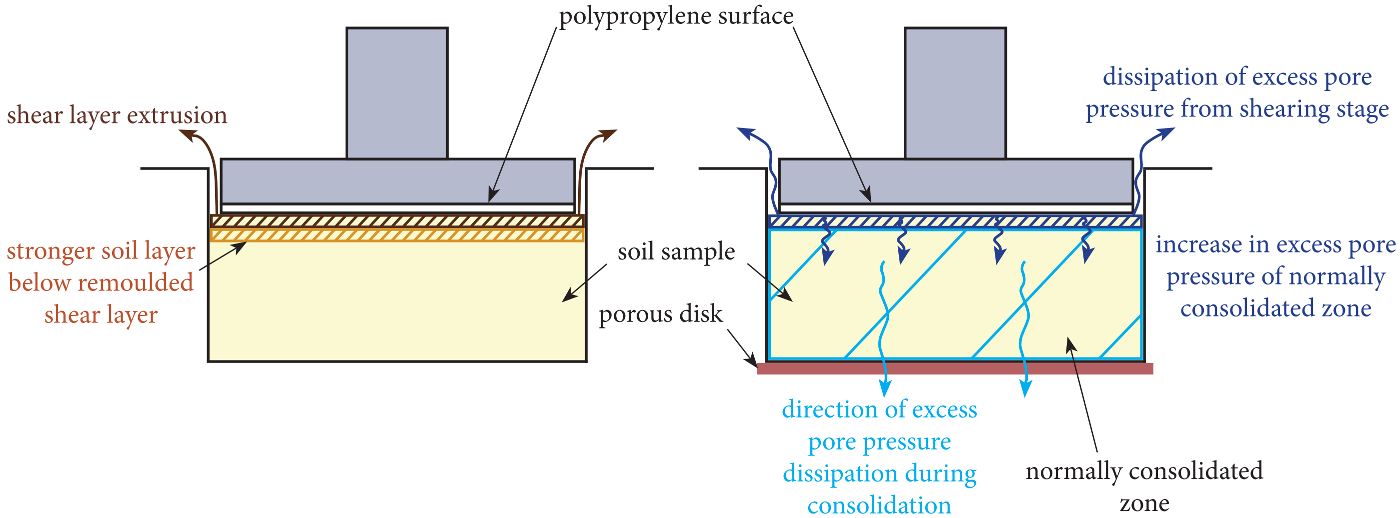


*Figure 4.4 - Schematic of the cross section of a soil-polypropylene interface test*

*Figure 4.3* also shows a decrease in friction angle for R = 21.62. This is a result of the interaction between interface sliding and simultaneous shear deformation depending on the three-dimensional surface profile. The decrease in friction angle indicates that the contribution to failure due to sliding has increased. The roughness widths have increased to a point where a clay layer formed by filling the crevices cannot be held stationary relative to the PP surface, contrary to the tests shown for R = 6.51 and R = 10.98. The shearing interface will therefore transition at points throughout the interface between soil-soil (Mode I) and soil-PP (Mode II). *Figure 3.8* shows the profile of this surface, with indentations frequently reaching 50 μm at millimetre spacings.

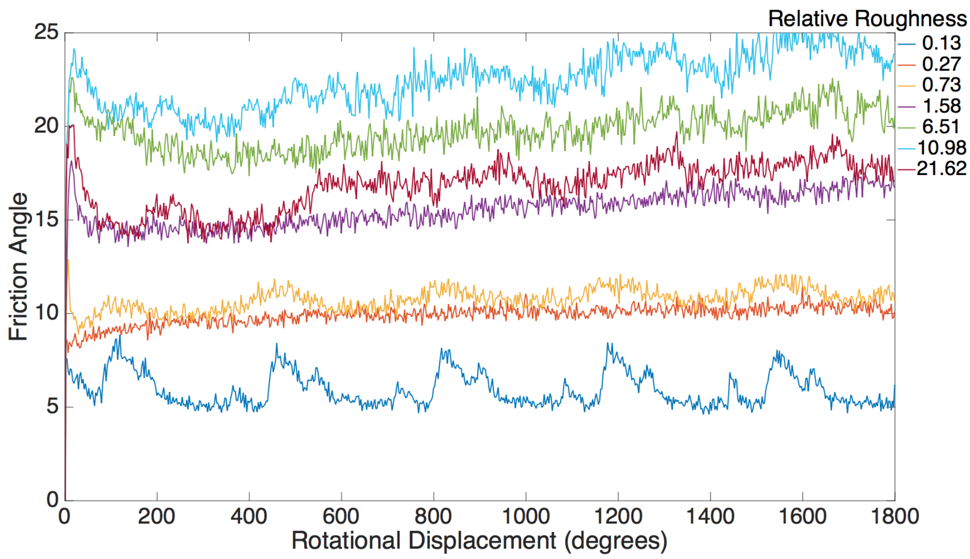


*Figure 4.5 - Plot showing change in shearing friction angle during 5th rotation cycle for the variety of relative roughnesses tested ($D_{50}$ = 0.7 μm)*

*Figure 4.5* corresponds to the final shearing cycle. Where interface sliding is the prominent form of failure (R = 0.13, 0.27 and 0.73), the increase in friction angle due to cyclic hardening is smaller due to a lower build up of excess pore pressures caused by shear deformations. As depicted in *Figure 4.4*, shearing causes a concentrated build-up of excess pore pressures in the shear zone, from which partial dissipation occurs into the normally consolidated zone underneath. Pausing stages between shear cycles allow excess pore pressures to dissipate and further consolidation to take place, hardening the soil sample. Larger relative roughnesses mobilise greater strain deformations and generate larger positive excess pore pressures. This results in the increased spreading of frictional resistances measured for the different relative roughnesses seen in *Figure 4.5*.

*Figures 4.6 and 4.7* show the results obtained for the first and fifth cycles of $D_{50}$ = 175 μm shearing. A one-dimensional median filter of order 50 has been applied to the output of each shearing test to reduce the noise observed. The undulating profiles arise from a scooping effect caused by lop-sidedness of the interface material, described in greater detail in §4.6.2. A distinct pattern in behaviour dependence on R is not discernible with the tests shown in *Figures 4.6 and 4.7*, largely due to the severe fluctuation of measurements.

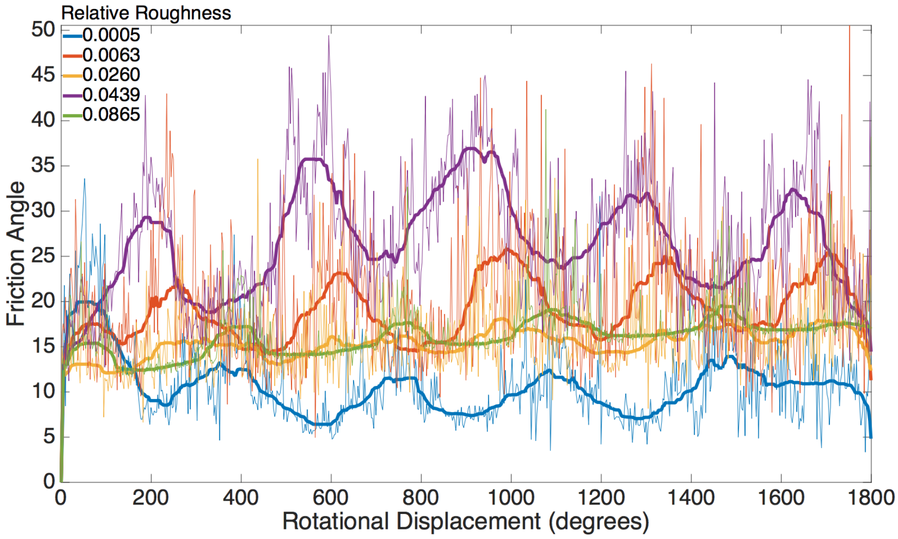


*Figure 4.6 - Plot showing change in shearing friction angle during 1st rotation cycle for the variety of relative roughnesses tested ($D_{50}$ = 175 μm)*

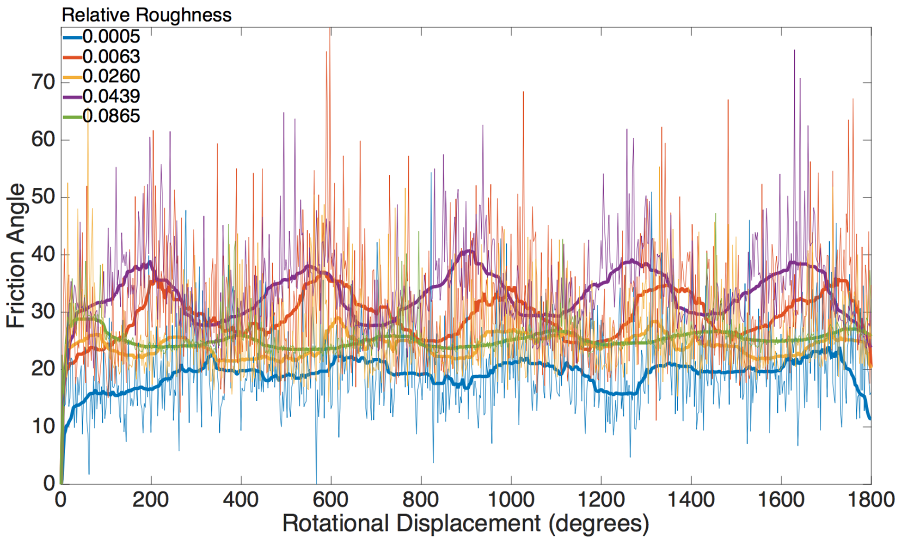


*Figure 4.7 - Plot showing change in shearing friction angle during 5th rotation cycle for the variety of relative roughnesses tested ($D_{50}$ = 175 μm)*

Comparing the test with R = 0.0005 shown in *Figure 4.6*, to the test with R = 0.13 shown in *Figure 4.3*, it can be seen that it is the clay particles that dominate the sliding failure behaviour of the clay-sand mix sample. This is from the observation that the friction angle is distinctly below tests of higher roughnesses, with minimum values within the fluctuations proximate to the sliding friction angle of the 100% clay sample. Sand grains floating in the clay matrix are generally unable to maintain a gripping force with the smooth interface to result in a significant increase in friction. Other than random occasions where a grain finds a notch in the surface, the sand rolls off the surface as shown in *Figure 4.8*.

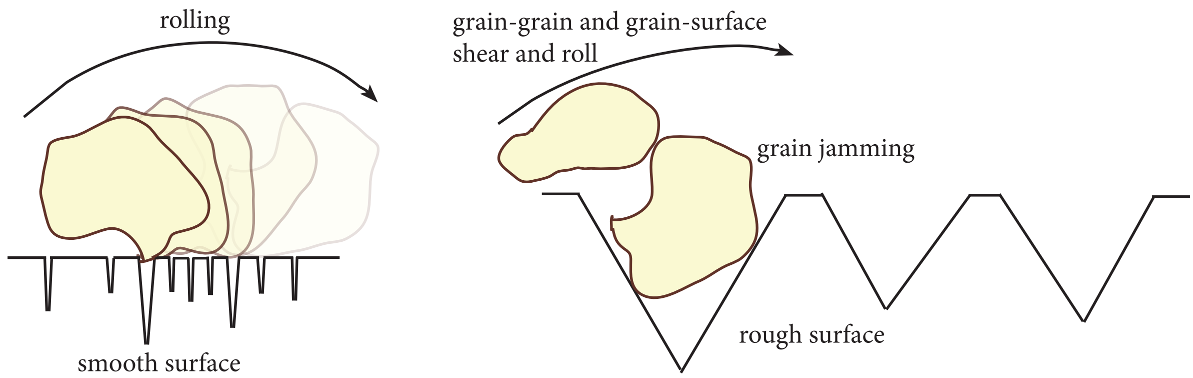


*Figure 4.8 - Schematic of sand grain interaction with relatively smooth (left) and rough (right) surfaces*

However, dissimilarly to the case presented in *Figures 4.3 and 4.5* for R = 0.13, the sliding frictional resistance for R = 0.0005, shown in *Figures 4.6 and 4.7*, increases between the first and last shearing cycles, by a factor of two. This is partly due to the reduced tolerance for soil extrusion arising from the presence of larger sand grain sizes, and the consequent increase in friction caused around the side of the interface disk as the soil extrudes out. Greater difficulty of sand extrusion compared to clay may also cause their segregation, leaving behind a greater proportion of sand grains to shear against the surface and have a more significant interaction. The greater the embedment, the more difficult extrusion becomes.

It is reasonable to speculate that the tests for R = 0.0260 and R = 0.0865 show reduced friction angles with less scatter due to improved compatibility between soil grain size and the specific three-dimensional topography of the PP surface. The clay matrix fills the crevices on the surface, creating a thin layer that remains stationary relative to the surface, such that the shearing interface becomes clay-clay. At these two roughnesses, sand particles may have jammed inside the valleys, breaking up the stationary clay layer and reinstating a degree of sliding failure that lowers the frictional resistance, as depicted in *Figure 4.8*.

### 4.2.2 Shearing Mechanism

*Figure 4.9* shows four polypropylene interfaces after testing. These photographs demonstrate the differences in soil-interface interaction between relatively smooth and rough surfaces, which help to explain the shearing mechanism taking place.

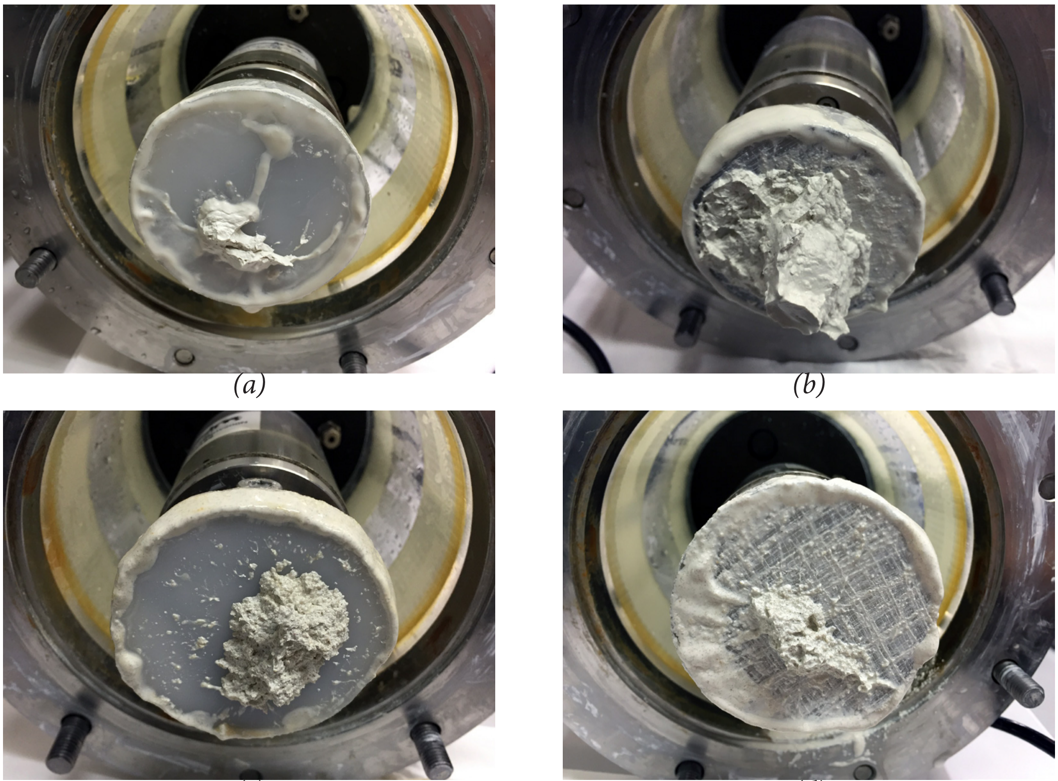

(a) (b) (c) (d)

*Figure 4.9 - Photographs of interface material after testing*
*(a) and (b) - Tests on $D_{50}$ = 0.7 μm; (c) and (d) - Tests on $D_{50}$ = 175 μm*
*(a) and (c) - Tests on Ra = 0.092 μm; (b) and (d) - Tests on Ra = 15.136 μm*

The angle of internal friction, as described by the Mohr-Coulomb friction model, is greater than the friction angle for sliding at the soil-pipeline interface. Smooth surfaces cause less shear deformation and disturbance in the soil sample because there is a smaller resistance to sliding. *Figures 4.9(a) and (c)* show that the smooth (Ra = 0.092 μm) polypropylene surfaces remain clear of soil particle residue. The large deposit of soil material seen is present as a result of the suction generated when the vertical stress decreases rapidly by lifting of the load cell at the end of testing.

As relative roughness increases, the soil next to the interface undergoes larger strains to flow over a coarser topography, leading to the failure plane moving further from the interface into the soil sample. *Figures 4.9(b) and (d)* show that the soil fills the crevices, creating a thin layer that remains stationary relative to the surface. The tests show that sole consideration of roughness average as the surface parameter does not fully capture the transition between the two failure mechanisms, particularly because it is a two dimensional parameter and is not specific to a distinct surface profile.

## 4.3 Cyclic Hardening

The phenomenon of cyclic hardening appears to affect tests differently depending on the shear failure mechanism. *Figure 4.10* shows the change in shearing friction angle with each shearing rotation cycle for R = 0.27, and *Figure 4.11* for R = 10.89.

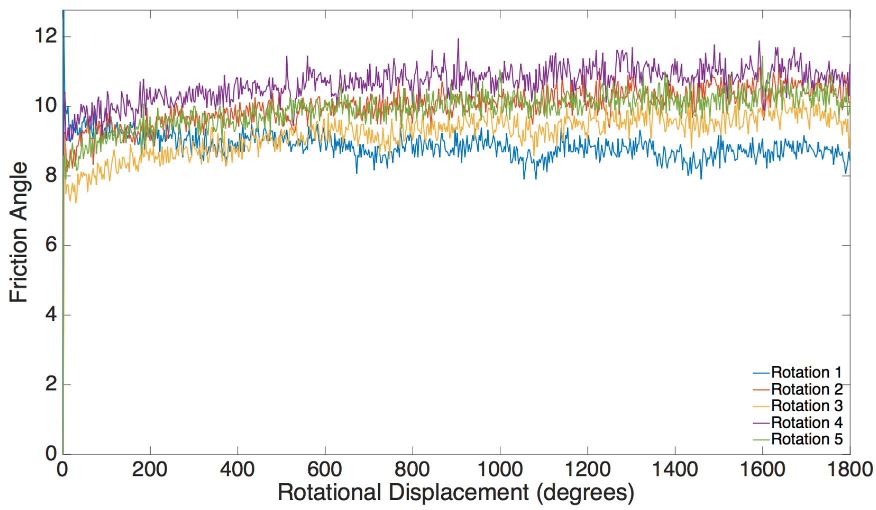


*Figure 4.10 - Plot showing change in shearing friction angle with each shearing rotation cycle for R = 0.27 ($D_{50}$ = 0.7 μm)*

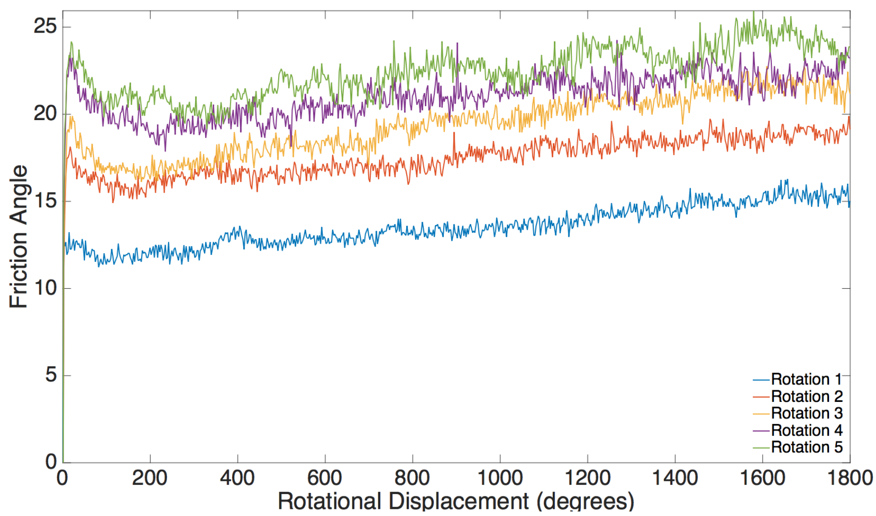


*Figure 4.11 - Plot showing change in shearing friction angle with each shearing rotation cycle for R = 10.98 ($D_{50}$ = 0.7 μm)*

The critical state model used to describe cyclic hardening in §2.1.2 applies to intergranular shearing within a soil structure. Therefore, in the case of the rough surface in *Figure 4.11*, where the shear failure occurs within the soil, the observed behaviour is as predicted. The degree of hardening depends on the pore pressure dissipation during pauses between cycles, generated during undrained shearing. With successive shearing cycles causing greater densification, the soil approaches the drained strength, as shown in *Figure 2.1*, and the consecutive increase in frictional resistance becomes smaller.

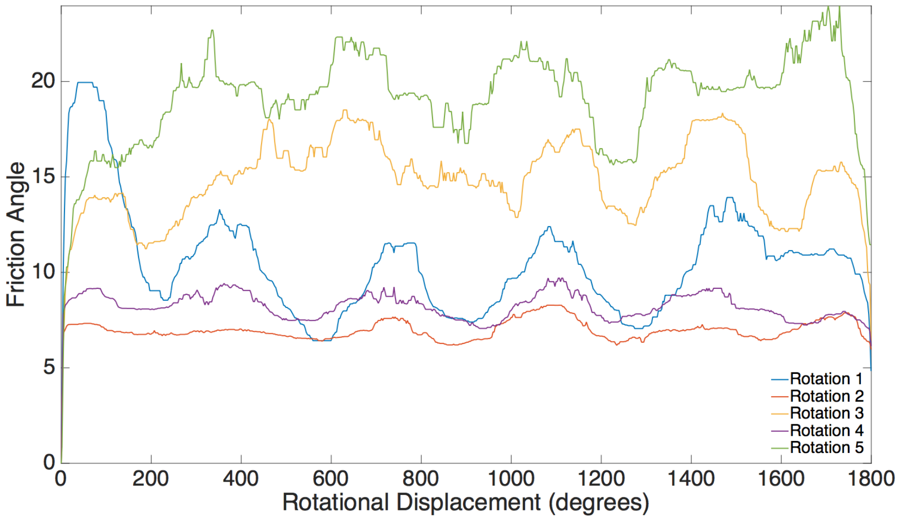


*Figure 4.12 - Plot showing change in shearing friction angle with each shearing rotation cycle for R = 0.0005 ($D_{50}$ = 175 μm) processed with a median filter*

*Figures 4.10 and 4.12* show cyclic changes in friction angle for sliding failures using $D_{50}$ = 0.7 μm and $D_{50}$ = 175 μm soils respectively. In these cases, hardening is observed between rotations in the same directions, with discontinuity in behaviour between reversals depending on the soil composition. The torsional resistance shown in *Figure 4.10* increases in rotations 2 and 4. The torsional resistance shown in *Figure 4.11* decreases in rotations 2 and 4.

*Figure 4.13* shows the same hardening behaviour as described for *Figure 4.11*, showing that the dominant failure mode in both of these tests occurs within the soil. This shows that the transition from full sliding to shear failure within the soil occurs when a stationary layer of the kaolinite clay particles forms by filling valleys in the surface topography.

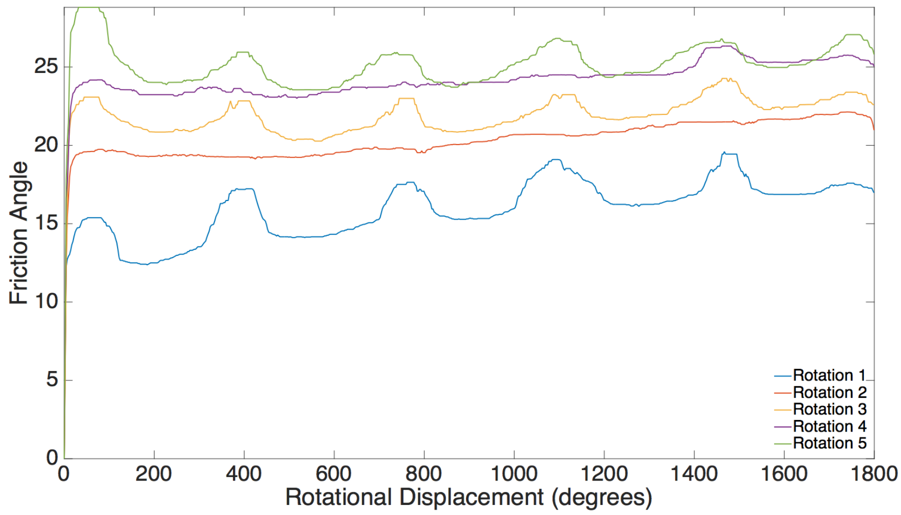


*Figure 4.13 - Plot showing change in shearing friction angle with each shearing rotation cycle for R = 0.0865 ($D_{50}$ = 175 μm) processed with a median filter*

It is important to consider the grading of the soil sample in addition to the median grain size, as a $D_{50}$ value may not encompass the reality of the intergranular forces present during shearing. In the tests considered here, the soil mixture corresponding to $D_{50}$ = 175 μm contains large Hostun sand grains floating in the matrix of very fine kaolinite particles. The sand grains have little to no intergranular contacts and are therefore a lot stiffer than their surroundings, requiring the fine matrix to absorb greater strains than those observed at the interface boundary to flow around the rigid particles. This translates to a larger generation of pore pressures and greater friction angles arising from cyclic hardening.

## 4.4 Breakout Resistance

For each test carried out, the Cam-Tor device was programmed to record at five-second intervals over the entire 37.5 hour running time. At a shearing rate of 0.5 degrees/second, the rotational displacement covered between recordings is 2.5 degrees. This corresponds to a shearing distance of 1.1 mm at the characteristic radius. Shearing typically reaches the residual resistance at distances of 6 - 10 mm (approximately 14 - 24 degrees), and therefore the sampling rate selected is able to provide sufficient clarity of torsional resistances during breakout prior to reaching the critical state.

### 4.4.1 Relative Roughness Effect

The torsional resistances measured at the beginning of the first and fifth shearing cycles for the tests carried out with 100% kaolinite clay are shown in *Figure 4.14*.

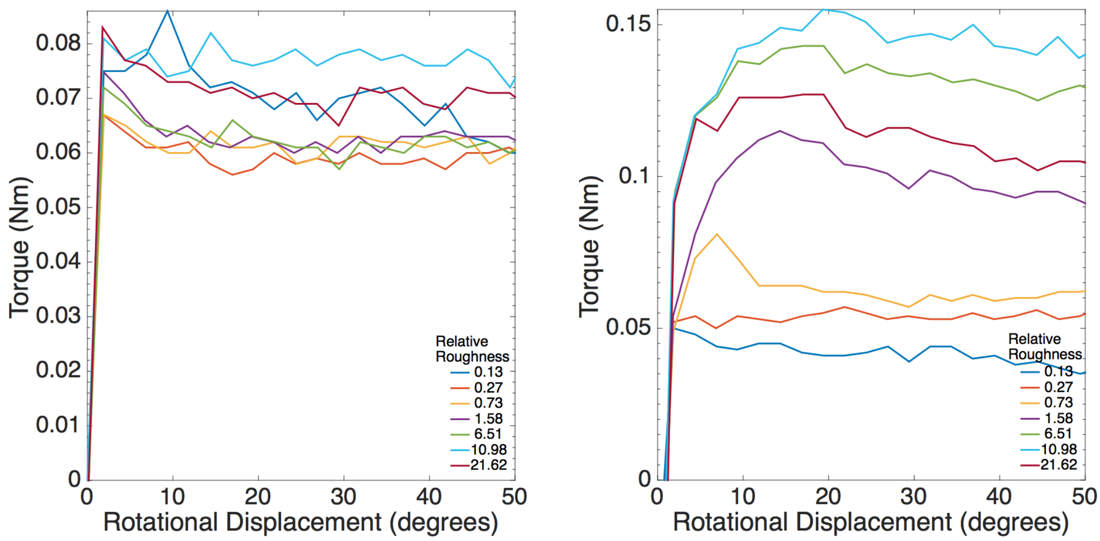


*Figure 4.14 - Breakout resistance corresponding to 1st (left) and 5th (right) rotation cycles for the range of relative roughnesses tested ($D_{50}$ = 0.7 μm)*

In the first shearing cycle, relative roughness has no effect on the mobilising displacement for breakout. The initial portion of the graph shows that from the onset, given by the first measurement at 2.5 degrees, there is a softening in resistance as failure is mobilised throughout the entire surface. It is important to recall that the velocity of individual particles against the interface increase from the centre of the sample to the outer circumference. Increasing R tends to increase the torque measured at breakout.

After several cycles of hardening, there is a clear change in the behaviour of the soil during breakout, dictated by the relative roughness. The values of R for which sliding failure dominates are the three smallest, and these show consistently that residual conditions are reached at almost immediate displacements, similar to the first rotation. The tests with higher values of R indicate that densification of the clay has occurred. Torque measurements show a peak shear strength followed by decay to residual values, a behaviour characteristic of dense soils. The strain deformation required for breakout increases with increasing R by up to ten times.

### 4.4.2 Rotation Cycle Effect

The effect of cyclic hardening on the breakout resistance is explored in *Figure 4.15* for a smooth (sliding failure) surface and a rough (failure within clay) surface.

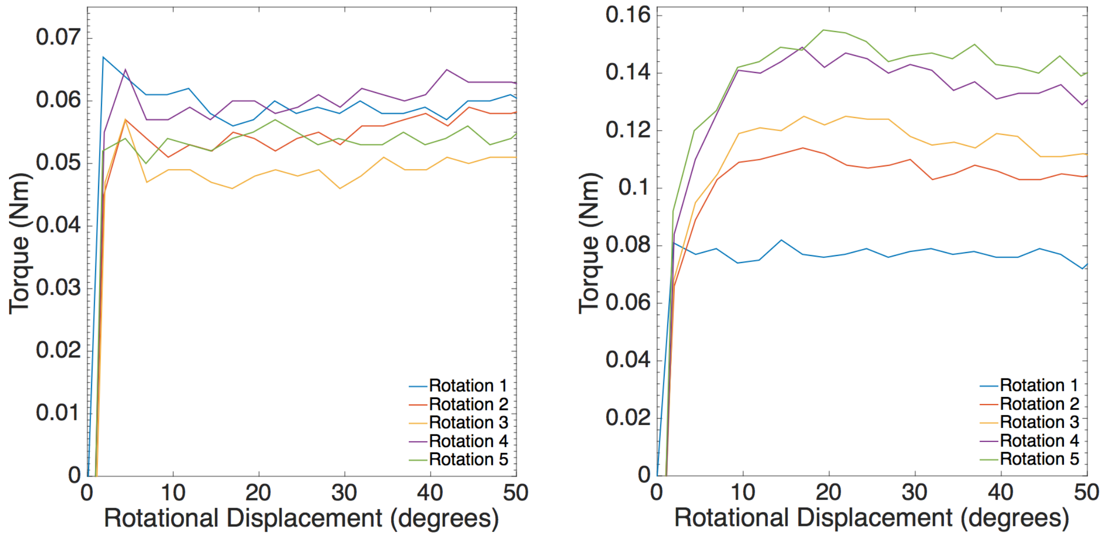


*Figure 4.15 - Breakout resistance change with each shearing rotation cycle for R = 0.27 (left) and R = 10.98 (right) ($D_{50}$ = 0.7 μm)*

For sliding failure, breakout for each rotation cycle occurs almost immediately. There appears to be no relationship between the breakout resistance and shearing cycle, as the soil sample does not undergo significant hardening. Differences arise due to random variations throughout the test.

For shear failure within the clay, cyclic hardening results in a greater breakout resistance, and a larger displacement is required to reach residual strengths.

## 4.5 Shearing Direction Discrepancies

The Cam-Tor device is very sensitive to the vertical alignment of the load cell and the fit of the top cap with the interface disk into the soil sample holder. A small number of of tests show inconsistencies between shearing cycles in opposite directions, as shown in *Figures 4.16 and 4.17*.

There are no physical changes in shearing at the soil-PP interface that can explain these discrepancies, and they may therefore be attributed to a mechanical failure in controlling the shearing rate, contact between the top cap and sample holder due to misalignment or imbalanced tightening of screws in the test set up.

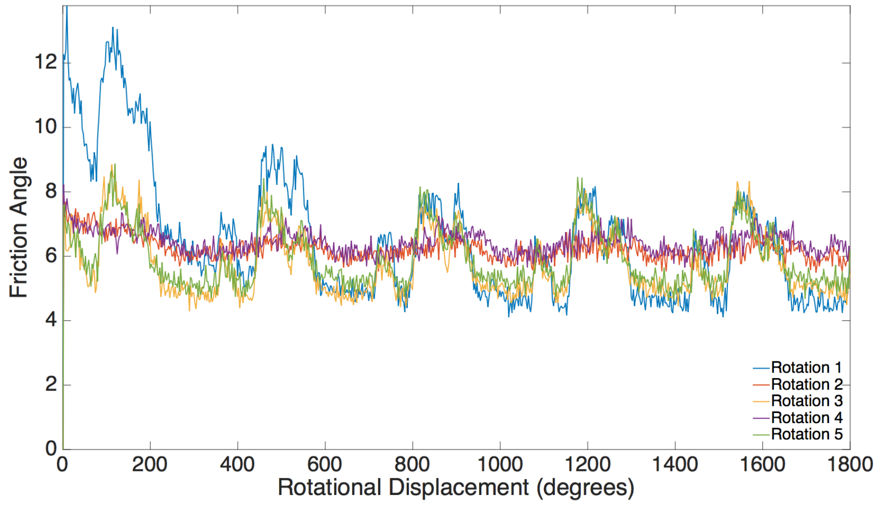


*Figure 4.16 - Plot showing change in shearing friction angle with each shearing rotation cycle for R = 0.13 ($D_{50}$ = 0.7μm)*

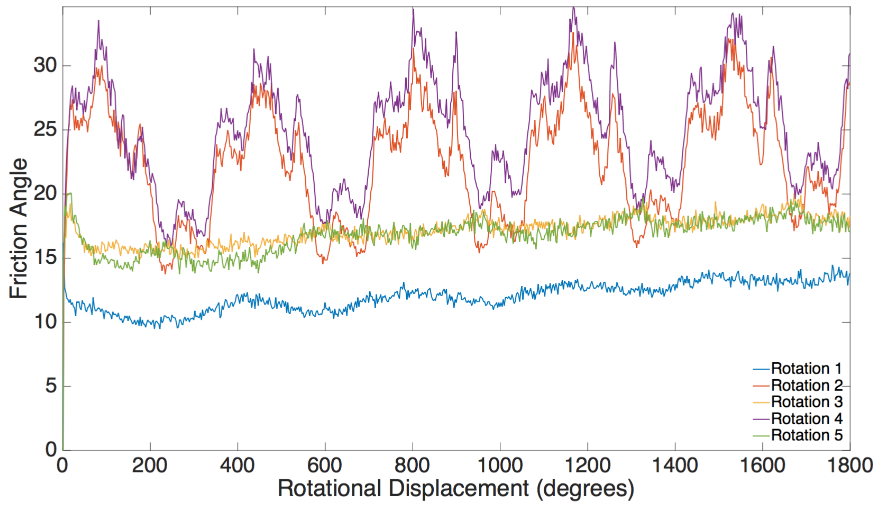


*Figure 4.17- Plot showing change in shearing friction angle with each shearing rotation cycle for R = 21.62 ($D_{50}$ = 0.7 μm)*

## 4.6 Axial Displacement

Measurement of axial displacement during the first one-dimensional consolidation and intermediate pauses between shearing cycles provides the best insight into pore pressure generation at the interface, as direct measurement is not currently possible. Axial compressions observed during rotations may provide insight into berm formation and the effects of increased confinement, as well as monitor the reduction in drainage length of the test specimen.

Curve fitting of the compression during the first one-dimensional consolidation stage, based on Terzaghi's Principle or parabolic isochrones solutions, provides an estimate for the coefficient of consolidation of the soil sample. This value can be used to assess the extent of consolidation occurring during each period of equalisation between shear cycles.

### 4.6.1 Shearing Rotations and Re-Consolidation Pauses

*Figures 4.18, 4.19, 4.20 and 4.21* show compressive axial displacements measured during four tests, where 'Rotation 1' is followed by 'Pause 1', followed by 'Rotation 2', and so on. *Figures 4.18 and 4.19* correspond to tests on 100% kaolinite clay samples, and *Figures 4.20 and 4.21* correspond to the kaolinite clay and Hostun sand mixture.

The rate of rotation is fast, and therefore, the assumption of fully undrained conditions is accurate. Increasing R increases the axial compression during shearing as a result of greater extrusion at the outer perimeter.

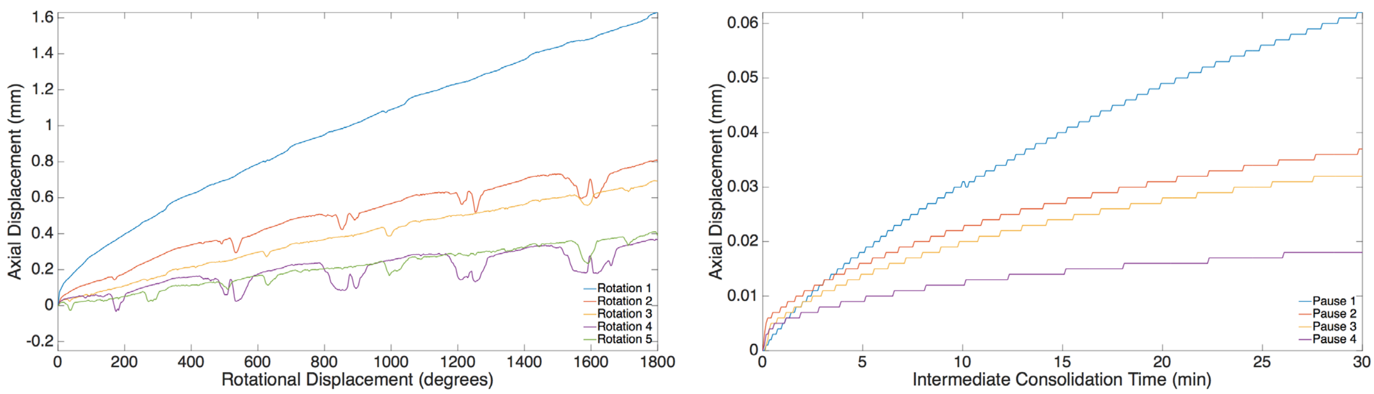


*Figure 4.18 - Compressive axial displacement measured during shearing rotation cycles (left) and during intermediate re-consolidation pauses (right) for R = 0.27 ($D_{50}$ = 0.7 μm)*

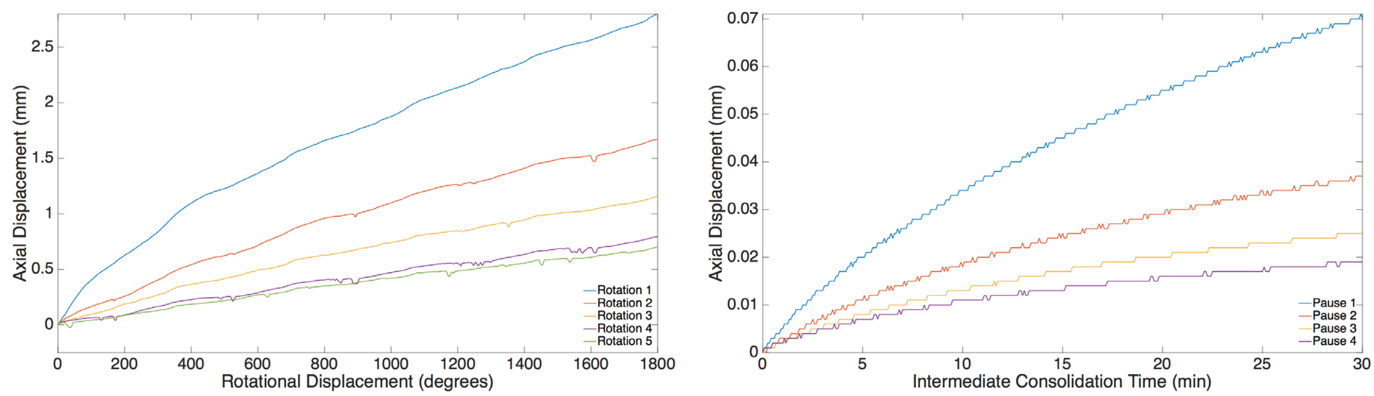


*Figure 4.19 - Compressive axial displacement measured during shearing rotation cycles (left) and during intermediate re-consolidation pauses (right) for R = 10.98 ($D_{50}$ = 0.7 μm)*

Comparing *Figures 4.18 and 4.19* shows that the reduction in drainage length caused by the greater extrusion results in faster excess pressure dissipation. This is observed by the 17% increase in axial displacement in the first pause. Recalling *Figures 4.10 and 4.11*, it can be seen that smaller axial displacements correspond to greater frictional resistance to rotation.

Larger positive excess pore pressures are also generated by the greater shear deformations caused with increasing R, which also lead to an initially larger rate of dissipation. The degree of axial compression during pauses scales with the pore pressure generated during the preceding rotations. A larger degree of dissipation generates a proportional increase in effective stress and shear strength of the soil. The relative decrease in axial displacements during consecutive pauses can therefore be seen to correlate with the relative increase in friction angle during successive shearing cycles shown in *Figures 4.10 and 4.11*.

*Figures 4.20 and 4.21* show greater axial compression, consistent with the explanation of incompatibility between sand grains in the clay matrix causing larger strains in the clay, described in

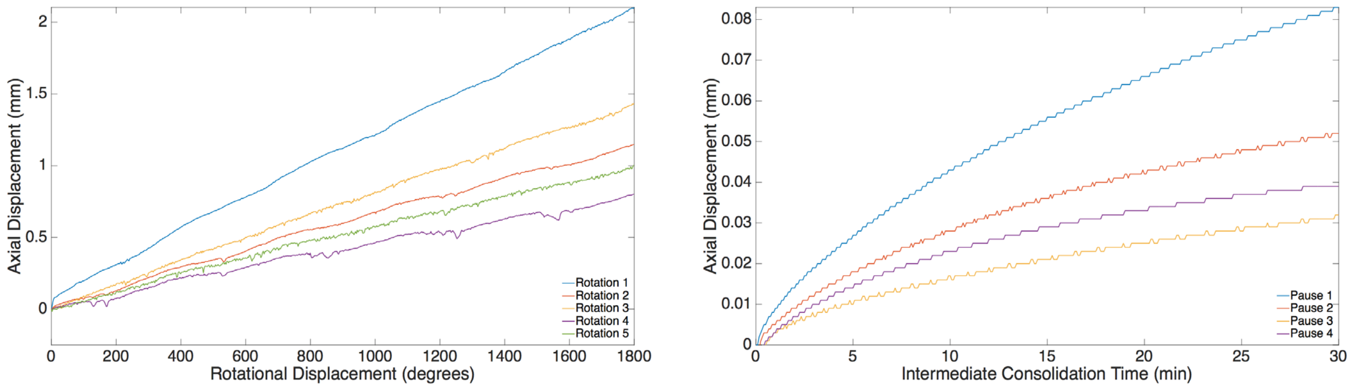


*Figure 4.20 - Compressive axial displacement measured during shearing rotation cycles (left) and during intermediate re-consolidation pauses (right) for R = 0.0005 ($D_{50}$ = 175 μm)*

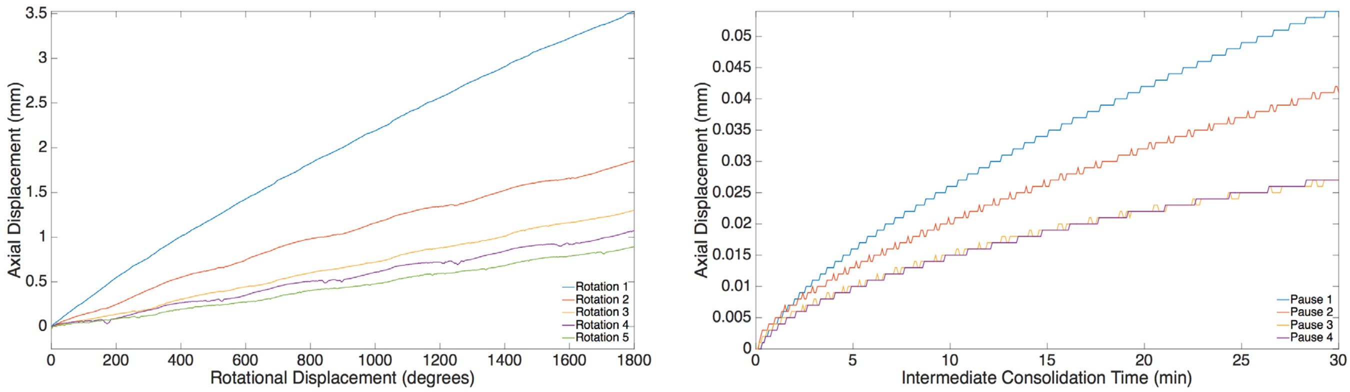


*Figure 4.21 - Compressive axial displacement measured during shearing rotation cycles (left) and during intermediate re-consolidation pauses (right) for R = 0.0865 ($D_{50}$ = 175 μm)*

§4.3, giving a proportional rise in excess pore pressures in the shear zone. *Figure 4.22* shows photographs depicting the differences in the volume extruded between the two types of soils tested.

*Figure 4.22 - Photographs showing extruded material at the end of tests on a sample made up of 100% kaolinite clay (left) and a sample of 50% kaolinite clay mixed with 50% hostun sand (right)*

The differences in axial compression during shearing rotations shown in *Figure 4.21*, for a test where failure occurs within the soil, are consistent with the relative magnitudes of the friction angles consequent of cyclic hardening observed in *Figure 4.13*.

Interpretation of the axial displacements for the case of sliding failure, given in *Figure 4.20*, is less clear, as excess pore pressures generated at the interface appear to be greater than those generated within the soil for when R is increased, as seen by the comparatively larger axial displacements during pause consolidations. Contrarily, the axial compressions during rotations in the sliding case are smaller than for shear failure within the soil. Further tests on sliding failure of the clay-sand mix are required to evaluate whether this apparent contradiction between axial displacements during rotations and intermediate pauses is anomalous to this test or indicative of a different induced pore pressure distribution and dissipation path. This is difficult to assess without direct pore pressure measurement in the shear zone.

Compression during rotation 1 is greater than during rotation 2, and *Figure 4.12* shows that this corresponds to a decrease in frictional resistance between the cycles. The same observation is made going from rotation 3 to rotation 4. Increases in friction angle are seen going from rotations 2 to 3, and rotations 4 to 5, and *Figure 4.20* shows that the corresponding compressions in these cases increase. This shows coupling between compression of the soil specimen given by the rate of extrusion and the frictional resistance at the interface.

### 4.6.2 Torque Measurement

*Figures 4.23 and 4.24* highlight a couple of subtleties that show that the measured output for torque does not fully encompass the frictional response, due to imperfections of the Cam-Tor device set up. These two figures compare the torque and axial compression measured over two distinct rotation cycles of the same test.

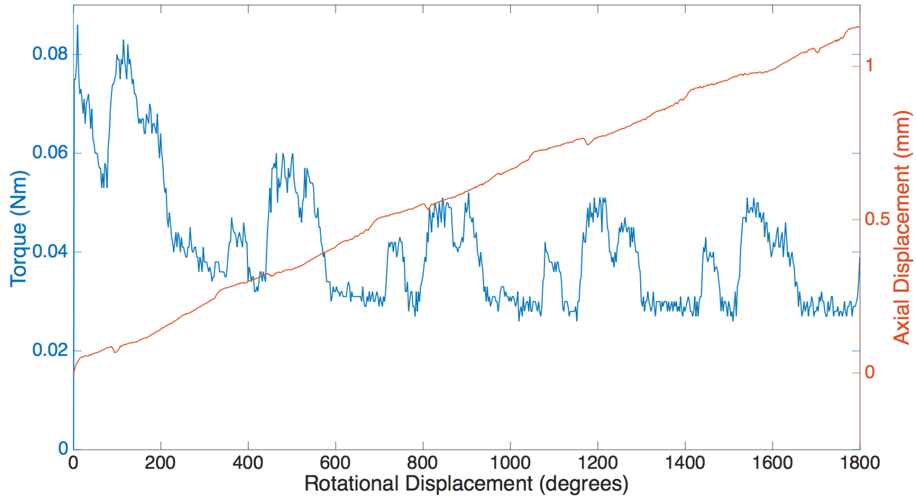


*Figure 4.23 - Plot showing torsional resistance to shearing and corresponding axial compression during 1st rotation cycle for R = 0.13 ($D_{50}$ = 0.7 μm)*

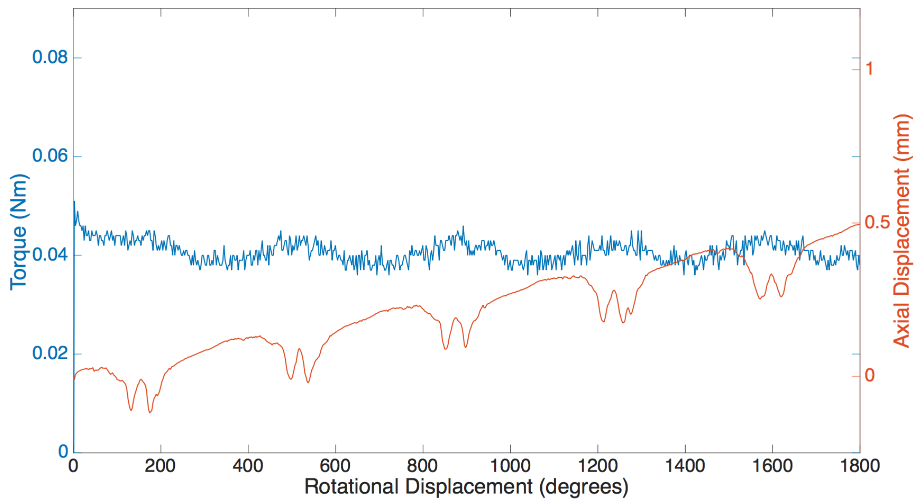


*Figure 4.24 - Plot showing torsional resistance to shearing and corresponding axial compression during 4th rotation cycle for R = 0.13 ($D_{50}$ = 0.7 μm)*

The errant cyclic pattern of torque, developed in the shearing cycle shown in *Figure 4.23*, is a result of scooping motions occurring at the clay-PP interface due to off-vertical alignment of the load cell. This causes the PP surface against which the soil is sheared to not be level with the workbench. Nevertheless, the axial displacement plot shows that there is no contact between the interface and sample holder as the compression increase is continuous.

*Figure 4.24* shows a torsional restraint with a small sinusoidal variation in magnitude, which remains relatively constant in value. The axial displacement reveals depressions in compression of approximately 0.2 mm at regular intervals. In this case, scooping may by causing undesirable contact, and the response of the load-controlled actuation is to lift the PP surface in order to maintain a constant pressure of 4 kPa. However, the cell is responding to changes in loading that are not from the soil reaction on the surface, and therefore the constant pressure applied to the soil sample may be misrepresented.

Securing the rigid pressure cell cylinder helps to rectify misalignment of the load cell, but some scooping still occurs due to adhesion of the PP sheet to the top cap not being perfectly flush. The top cap does not accommodate the rocking effect on the surface due to scooping, as the joint to the load cell needs to be rigid for accurate control of axial displacement.

## 5 Conclusions

This study aimed to obtain greater insight into the effects of varying the relative roughness at the interface on the frictional resistance, and assess how these correlate with the modes of failure.

- Use of relative roughness as a design parameter:

Relative roughness is defined as the ratio between the roughness average of the surface and the median particle size of the soil sample ($D_{50}$). When testing the effect of relative roughness on frictional resistance, it is important to assess whether these two parameters capture the observed behaviour during shearing.

Roughness average is a two-dimensional parameter that is not specific to a distinct surface profile, and $D_{50}$ fails to recognise the incompatibility of a mixture of sand grains within a clay matrix. Tests show that the combination of these parameters does therefore not always fully describe the transition between failure due to sliding at the interface and shearing within the soil.

- Tests carried out on samples containing 100% kaolinite clay:

The tests of different relative roughnesses showed that the mechanism of failure can be detected during the first cycle of torsional resistance. The lowest measured friction angle corresponds to sliding failure at the interface, and the highest corresponds to shear failure within the clay sample. Intermediate values show varying degrees of a combination of these two mechanisms.

The dominating mode of failure becomes clearer through cycles of hardening. Increasing surface roughness leads to greater remoulding of the soil top layer and a larger generation of excess pore pressures. Intermediate pauses between shearing cycles allow pore pressures to dissipate, densifying the clay to have a higher frictional resistance in successive cycles. This greater strain deformation is characteristic of shear failure within the soil. Where interface sliding is the prominent form of failure, the increase in friction angle due to cyclic hardening is small due to a lower build up of excess pore pressures.

Increasing the relative roughness causes faster extrusion of the shear layer, at the outer perimeter of the contact area. The shear layer, having been remoulded to a residual strength, is weaker than the normally consolidated zone underneath. Extrusion consequently causes a gradual increase in torsional resistance as the stronger normally consolidated soil is introduced into the shearing zone. Therefore, as the shear displacement length increases, tests show an increase friction angle, and more significantly so as the relative roughness is increased.

The frictional resistance does not appear to plateau with increasing relative roughness, as the literature suggests. The highest relative roughness tested showed a decrease in frictional resistance in one direction of shearing, and an increase in the reverse direction. This is a result of the interaction between interface sliding and shear deformation occurring simultaneously depending on the three-dimensional surface profile.

For the cases where the governing mode of failure is shearing within the soil, the general increase in strength due to cyclic hardening, caused by increasing the relative roughness, causes breakout to residual frictional resistance to require larger displacements.

- Tests carried out on samples containing 50% kaolinite clay and 50% Hostun sand:

Due to a difference in size of approximately three orders of magnitude, the clay-soil mixture tested is incompatible. This means that sand grains have little to no intergranular contacts and are therefore a lot stiffer than their surroundings. The fine clay matrix is therefore required to absorb greater strains than those observed at the interface boundary to flow around the rigid particles.

Larger strain deformations cause a greater build up of positive excess pore pressures and the effect of cyclic hardening is more significant for the clay-sand mixture. A greater amount of extrusion during shearing is also observed.

This incompatibility renders the use of $D_{50}$ insignificant for these tests. Clay particles are shown to dominate the response, giving friction values comparable to tests involving 100% kaolinite clay soils, despite the $D_{50}$ value suggesting relative roughnesses of up to three orders of magnitudes smaller.

Inclusion of sand gives more scattered results, and distinct bands of failure mechanisms are not obvious, except in the case of sliding. Sand grains floating in the clay matrix are generally unable to maintain a gripping force with a smooth interface to result in a significant increase in frictional resistance.

Increasing the roughness average of the surface gives mixed results for frictional resistance, as the degree of simultaneity between sliding failure and shear failure within the soil depends on the compatibility between the soil grain sizes and the specific three-dimensional topography of the interface.

Sand particles cause changes in the transition between the mechanisms observed for samples containing only clay. Frictional resistance increases from sliding at the soil-PP interface to shear failure within the soil as roughness increases. The clay matrix fills the crevices on the surface, creating a thin layer that remains stationary relative to the surface, such that the shearing interface becomes clay-clay. With greater roughness widths, sand particles may also jam inside the valleys, breaking up the stationary clay layer and reinstating a degree of sliding failure that lowers the frictional resistance.

# 6 Recommendations for Future Work

Further options for roughening the polypropylene material surface can be explored. Texturized 3D printed surfaces or wire meshes adhered to the plastic can be designed and tested to compare different surface profiles with the same roughness average. This can be used to investigate what surface topographical features specifically influence compatibility with the soil particle sizes, or trigger the transition between failure modes.

Measurement of the surfaces using a 3D optical or scanning profilometer would further improve understanding of the friction along the path of particle movement, to verify the conversion of torsional friction at the characteristic radius to an equivalent resistance along a straight path.

The effects of soil strengthening from cyclic hardening can be exploited to predict the axial pipeline resistance. The design of a textured surface that produces greater strains and excess pore pressures in the soil and reaches peak hardened strength in fewer shearing cycles can be investigated.

The transitions between the modes of failure have been hypothesised in order to explain the results observed. Work can be done to modify the sample holder to provide visual access to the shear zone. Particle Image Velocimetry analysis can be incorporated into the test plan as a way to trace particle movement between failure modes and observe the evolution of the shear zone thickness.

It would be a great topic of interest to continue work on samples of clay-sand mixes of different proportions, to see how varying the sand content in the clay matrix influences the transitions between failure modes.

Finally, it would be of value to explore development of a robust method for analysing the pore pressures generated in the shear zone, either by analysing consolidation curves from the intermediate pausing stages or by continuing past attempts to incorporate pore-water pressure transducers.

## 7 References


Allen, E., (2015, 02). "Subsea production technology development." *E & P*.

Borges Rodriguez, A., Draper, S., Boylan, N. P., Begaj, L., Bransby, M. F., (2014). "Pipe-soil interaction during cyclic buckling: The importance of site-specific seabed properties." *Proceedings of the ASME 2014 33rd International Conference on Ocean, Offshore and Arctic Engineering. San Francisco.*

Bruton, D. A. S., Carr, M., White, D. J., (2007). "The influence of pipe-soil interaction on lateral buckling and walking of pipelines – the SAFEBUCK JIP." *Proceedings of the 6th International Offshore Site Investigation and Geotechnics Conference: Confronting New Challenges and Sharing Knowledge. London.*

Carneiro, D., White, D. J., Danzinger, F. A. B., Ellwanger, G. B., (2015). "Excess pore pressure redistribution beneath pipelines: FEA investigation and effects on axial pipe-soil interaction." *Frontiers in Offshore Geotechnics III. London: Taylor and Francis Group.*

Carsodo, C. O., Amaral, C. S., Ochi, V. T., (2015). "The soil strength degredation influence in the axial pipe-soil resistance." *Frontiers in Offshore Geotechnics III. London: Taylor and Francis Group.*

Colliat, J. L., Dendani, H., Puech, A., Nauroy, J.-F., (2011). "Gulf of Guinea Deepwater Sediments: Geotechnical Properties, Design Issues and Installation Experiences." *Proceedings of the 2nd International Symposium On Frontiers in Offshore Geotechnics (ISFOG-II), Perth, Australia, Nov 8–10, 2010, pp. 59–86.*

Fyrileiv, O., Aamlid, O., Venås, A., Collberg, L., (2013). "Deepwater pipelines – status, challenges and future trends." *IMech E, Journal of Engineering for the Maritime Environment, 227(4), 381-395.*

Ganesan, S., Kuo, M. Y. –H., Bolton, M. D., (2014). "Influences on pipeline interface friction measured in direct shear tests." *ASTM Geotechnical Testing Journal, Vol 37.*

Hill, A. J., White, D. W., Bruton, D. A. S., Langford, T., Meyer, V., Jewell, R., Ballard, J. -C., (2012). "A New Framework for Axial Pipe–Soil Resistance, Illustrated by a Range of Marine Clay Datasets." *Proceedings of 7th SUT Offshore Site Investigation and Geotechnics International Conference, London, UK, Sept. 12–14, pp. 367–377.*

Hill, J., White, D. J., (2015)., "Pipe-soil interaction: Recent and future improvements in practice." *Frontiers in Offshore Geotechnics III. London: Taylor and Francis Group.*

Hodder, M. S., Cassidy, M. J., (2010). "A plasticity model for predicting the vertical and lateral behaviour of pipelines in clay soils." *Géotechnique 60, No. 4, 247-263.*

Kaye, D., (1996). "Lateral Buckling Of Subsea Pipelines: Comparison Between Design And Operation." *Society of Underwater Technology, Aspect '96: Advances in Subsea Pipeline Engineering and Technology, 27-28 November, Aberdeen, UK.*

Kuo, M. Y. –H., Bolton, M. D., (2014b). "Shear tests on deep-ocean clay crust from the Gulf of Guinea." *Géotechnique, 64(4): 249-257.*

Kuo, M. Y. –H., Vincent, C. M., Bolton, M. D., Hill, A., Rattley, M., (2015). "A new torsional shear device for pipeline interface shear testing." *Frontiers in Offshore Geotechnics III. London: Taylor and Francis Group.*

Lemos, L. J. L., Vaughan, P. R., (2000). "Clay-Interface Shear Resistance." *Geotechnique, Vol. 50, No. 1, pp. 55–64.*

Meyer, V. M., Dyvik, R., White, D. J., (2015). "Direct shear interface testes for pipe-soil interaction assessment." *Frontiers in Offshore Geotechnics III. London: Taylor and Francis Group.*

Min, L. J., (2015). "Interface Shear Testing for Pipelines, Fourth-year undergraduate project." *University of Cambridge.*

Najjar, S. S., Gilbert, R. B., Liedtke, E., McCarron, B., Young, A. G., (2007). "Residual Shear Strength for Interfaces Between Pipelines and Clays at Low Effective Normal Stresses," *ASCE J. Geotech. Eng., Vol. 133, No. 6, pp. 695–706.*

Oliphant, J., Maconochie, A., (2007). "The axial resistance of buried and unburied pipelines." *Proceedings of the 6th International Offshore Site Investigation and Geotechnics Conference: Confronting New Challenges and Sharing Knowledge. London.*

Pederson, R. C., Olson, R. E., Rauch, A. F., (2003). "Shear and Interface Strength of Clay at Very Low Effective Stress." *Geotech. Test. J., Vol. 261, pp. 71–78.*

Randolph, M. F., White, D. J., Yan, Y., (2012). "Modelling the axial soil resistance on deep-water pipelines." *Géotechnique 62, No. 9, 837-846.*

Schofield, A., Wroth, P., (1968). "Critical state soil mechanics". *McGraw-Hill, New York.*

Smith, V., Kaynia, A. M., (2015). "Pipe-soil interaction under rapid axial loading." *Frontiers in Offshore Geotechnics III. London: Taylor and Francis Group.*

Terzaghi, K., (1996). "Soil mechanics in engineering practice." *John Wiley & Sons.*

Tsuchida, T., (2001). "Settlement of Pleistocene clay in costal area, the reason, prediction and measure." *Soft Soil Engineering, Swets & Zeitlinger.*

Tsuchida, T., Gomyo, M., (1995). "Unified model of e-log ρ relationship with the consideration of the effect on initial void ratio." *Proc. Of International Conference on compression and consolidation of clayey soil.*

Wang, K. Li, L., Yuan, F., (2015). "Large scale experiments on the riser-soil interaction in clay." *Frontiers in Offshore Geotechnics III. London: Taylor and Francis Group.*

White, D., Campbell, M. E., Boylan, N., Bransby, M. F., (2012). "A New Framework for Axial Pipe-Soil Interaction Illustrated by Shear Box Tests on Carbonate Soils." *Proceedings of the 7th International Conference of the Society for Underwater Technology, London, UK, Sept 12–13, Vol. 1, pp. 379–387.*

## Appendix – Risk Assessment Review

The risk assessment conducted prior to the commencement of testing reflected the potential hazards of using the Cam-Tor device very well. These were drafted after extensive communication with the previous user and developer of the device. The series of steps required for carrying out each test were well understood for before, during and after each testing sequence. Instruction was provided on how to programme the tests through the provided software, whereby actuator control for load application and base rotation could be carried out safely.

The most significant hazard encountered involved tightening and loosening the screws in the device for setting up and taking down tests. These required significant strength, which initial assessment underestimated.

The working area was very spacious and maintained in a clean and tidy state. This eliminated all tripping hazards and made manoeuvring around the area very manageable.

In retrospect, the risk assessment could have been extended to the wider laboratory area, and not only evaluating the risks of using the Cam-Tor device itself, as soil samples were moved between different specific locations for various stages of analysis.